Title
Modeling mixed conductivity in solid-state electrolytes

Author
ADELSTEIN, NICOLE

Publication Date
2012

Modeling mixed conductivity in solid–state electrolytes

by
Nicole Carol Mei Lin Adelstein

A dissertation submitted in partial satisfaction

of the requirements for the degree of

Doctor of Philosophy

in

Engineering – Materials Science and Engineering

in the

Graduate Division

of the

University of California, Berkeley

Committee in charge:
Professor Lutgard C. De Jonghe, Chair
Professor Mark D. Asta
Professor Jeffrey A. Reimer

Fall 2012

Abstract

Modeling mixed conductivity in solid-state electrolytes

by
Nicole Carol Mei Lin Adelstein

Doctor of Philosophy in Engineering – Materials Science and Engineering
University of California, Berkeley

Professor Lutgard C. De Jonghe, Chair

The overarching goal of the first-principles computational studies presented in this dissertation is to better understand and predict charge carrier interactions in mixed conductors. Rare-earth phosphates and hematite are chosen as example insulators which show reasonably high proton and polaron conductivity, respectively. Rare-earth phosphates are not yet used commercially, but show promise as intermediate temperature fuel–cell electrolytes, so a first-prinicples atomic-level understanding of transport in these materials will enable engineering of their properties. Due to close collaborations with experimentalists working in synthesis and characterization of rare-earth phosphates via impedance, X-ray photoemission, and NMR spectroscopy, the density functional theory (DFT) studies are compared directly to experimental measurements.

Significant charge carrier concentrations are created in these materials by aliovalent doping, which can significantly increase the activation energy barrier for transport through the material. In this thesis, the interaction of protons and Ba-dopants in $LaPO_4$ is investigated and the X-ray photoemission spectrum of $CePO_4$ is interpreted via its calculated electronic structure, showing that hole small-polarons on Ce ions are stable defects. Finally, a new method for calculating small-polaron mobilities in crystals with DFT plus a Hubbard-U term is presented and found to work well for electron small-polaron mobilities in hematite.

Acknowledgments

The research presented in this dissertation was made possible by my many teachers, starting with the first and most essential, my parents, Monica and David.

Many thanks go to following people who allowed me the curiosity and confidence to pursue my Ph.D.: in high school – Mr. Groves and Josh W, at Reed – Maggie G, Dan G, David G and johnny p, in Portland – Joy C and Kevin S, at Cal and LBL – Jeff R, Mark J, Isaac T, Alexey Z, Alejandro L, and Hannah R, my scientific mentors – Mark A and Jeff N, and Lut DJ, the best possible thesis advisor I could have imagined.

I hope I have expressed my gratitude in more ways than these simple words.

Contents

List of Figures

List of Tables

Chapter 1

Introduction

1.1 Motivation

The intersection of experiment, theory, and simulation is fertile ground for the development of complex materials systems. While the focus of this dissertation is on simulating proton and mixed conductivity in rare–earth phosphates, the results have wide–reaching impact in the fields of modeling ionic and polaronic conductivity and rare–earth compounds. Rare–earth phosphates, in particular $LaPO_4$, have been researched since the early 1990s as solid–state electrolyte membranes for intermediate temperature hydrogen fuel cells. The crystalline electrolyte is doped in order to increase proton concentration, but does not yet have high enough conductivity to compete with current energy production systems. Thus, we are motivated to understand proton conductivity in $LaPO_4$ and other rare–earth phosphates in order to engineer higher conductivity, interpret experimental measurements, and predict better materials.

In 2007 Congress approved millions of dollars for energy research under the Advanced Research Programs Agency–Energy (ARPA–E)[1] to address our global need to find cheaper and cleaner energy sources and storage. A significant effort has been made in developing fuel cells to reduce our dependence on fossil fuels in internal combustion engines and coal power plants; currently, fuel cells are found in buses and as stationary back–up power generation. The hydrogen fuel cells used in buses operate at relatively low temperatures (less than 200°C) due to the need to keep them hydrated. At the opposite temperature extreme, stationary solid oxygen fuel cells operate most efficiently at around 800°C. Since very few proton conducting electrolyte membranes that operate at intermediate temperatures between these two extremes, called the Norby Gap[2], have been tested, they are the focus of this research and many others. At the intermediate temperature range and above, fuel cells benefit from using non–noble catalysis (noble catalysts like Pt are required for low temperature nafion based fuel cells[3]) and in–situ reforming of biofuels. But the drawback of solid–oxide fuel cells (SOFC) that operate at such high temperatures as 700–1000°C is that they suffer from corrosion, require long start–up times, and can have mechanical problems due to the mismatch of different components after thermal–expansion. Intermediate temperature proton–conducting electrolytes are desired to allow thermal cycling and non–noble catalysts.

The electrolytes with the highest conductivities in the intermediate temperature range are barium zirconate and barium cerate ($BaZrO_3$ and $BaCeO_3$)[4], both perovskites with conductivities around 10^{-3} S/cm at 300°C. However, both have highly resistive grain boundaries and growing single crystal electrolytes to remove the grain boundaries is too expensive, so another alternative must be found. Investigation into rare–earth phosphates is inspired by the high conductivity of phosphoric acid, of 0.45 S/cm at 100°C[5]. Like the Nafion used in automotive fuel cells, phosphoric acid electrolytes break down at temperatures over 200°C [5], which limits the efficiency of phosphoric acid fuel cells and requires the use of Pt catalysts. Phosphate–based materials with high melting temperatures, like monazite, could increase grain boundary conductivity by incorporating extra phosphates into the grain boundaries to create phosphoric acid like environments. The mineral monazite has a melting temperature of 2057°C and is an orthophosphate solid solution of Ce and La with Th and Nd impurities[6][7]. Rare–earth orthophosphates are considered to be ionic ceramics with the 3- charged phosphate anions charge balancing the 3+ rare–earth cations (RE), as shown in Figure 1. These phosphate groups can link by sharing an oxygen to create a pyrophosphate impurity and with smaller RE:P ratios give the metaphosphates (REP_3O_9) and ultraphosphates (REP_2O_5) with phosphate chains.

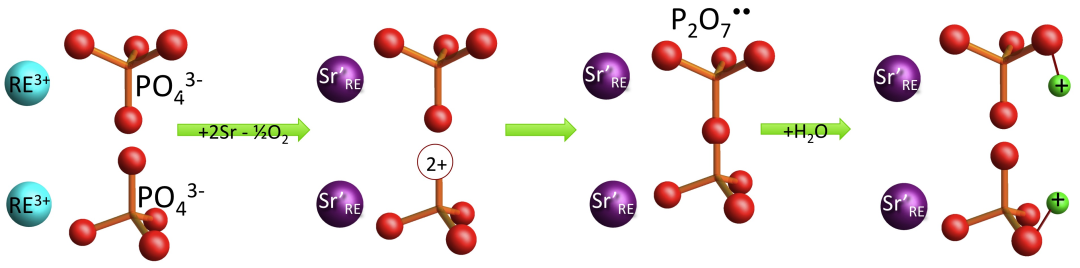

Figure 1.1: The phosphate group, consisting of oxygen (red) tetrahedra around a phosphorus ion, has a nominal 3 minus charge. The cation, La or Ce (blue), charge compensates with a 3 plus charge. An oxygen vacancy has a 2+ charge with is charge compensated by the effective negative charge of the two Sr_{RE} (purple).

The highest proton conductivity measured for Sr–doped $LaPO_4$ is $1.55*10^{-5}$ S/cm at 800°C but a range of conductivities have been reported (Figure 2). For Sr–doped $CePO_4$, the conductivity at 800°C is $1.63*10^{-3}$ S/cm [8], orders of magnitude higher than $LaPO_4$, but is generally accepted to be caused by hole–polaron conductivity. Such electronic conductivity (hole) is possible in $CePO_4$ compared to $LaPO_4$ because Ce^{3+} has a lone 'f'–electron which can be ionized to create Ce^{4+}, where as La^{3+} has a filled 5p shell and empty 4f shell.

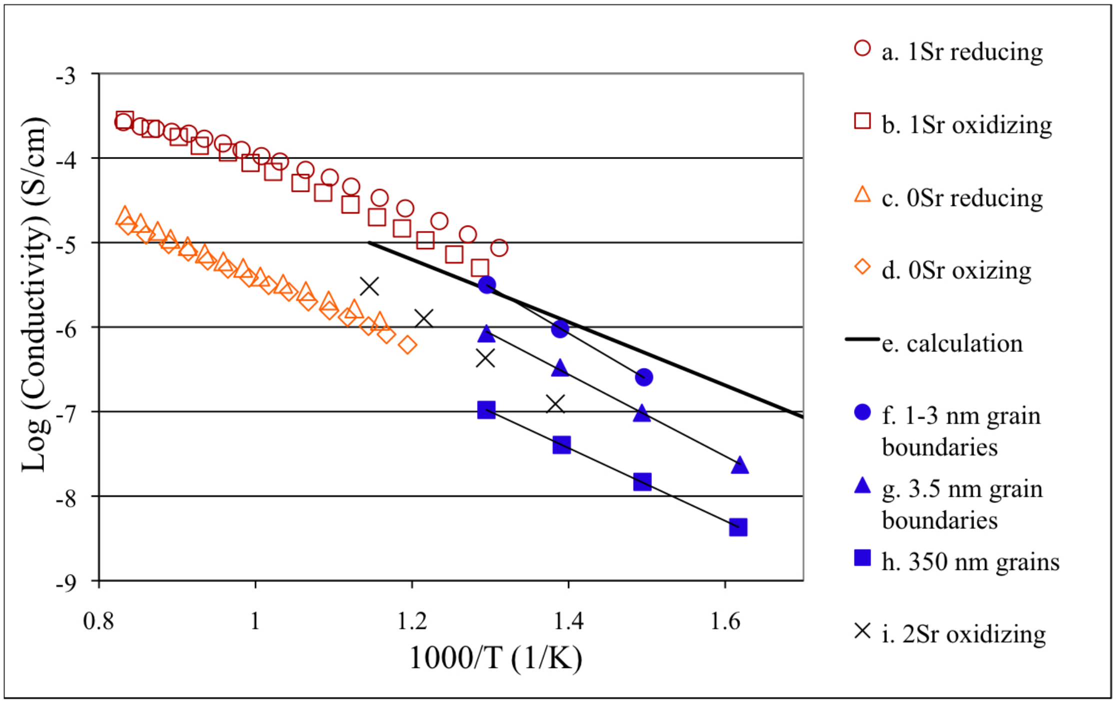

Figure 1.2: Various proton conductivity measurements in $LaPO_4$ have been reported. 0Sr indicates no Sr–doping while 1Sr indicates 1% Sr–doping, etc. The blue data are from a microstructure–study, where the grain sizes were varied. Data f) have 3μm grains and data g) have 20 μm grains. The sample with 350 nm grains was not sintered to created larger glassy grain boundaries. References are as follows a–d)[8] e)[9] f–h)[10] i) Personal data from H.L. Ray.

The electronic conductivity in cerium orthophosphate initially ruled it out as a fuel cell electrolyte since it will cause a partial short circuit and lower the open circuit voltage (OCV), but our current research may indicate that some electrical conductivity can be tolerated. Here, a brief summary of fuel cell thermodynamics will be illustrative. In a fuel cell, electrical power is derived from the reaction of the fuel with oxygen and the change in Gibbs free energy from that reaction (or free energy of formation). For example in a hydrogen fuel cell:

$$H_2 + \frac{1}{2}O_2 \xrightarrow{\text{exothermic}} H_2O. \tag{1.1}$$

The hydrogen and oxygen gases are separated by the ionically–conducting electrolyte membrane (so they do not combust directly), which should be insulating so that the H_2 fuel is oxidized and electrons are forced outside the electrolyte to do work. Protons are drive across the electrolyte by a gradient in electochemical potential from the formation of water upon combination with O_2 at the cathode.

The open circuit voltage is proportional to the negative of the free energy of formation of water from H_2 and O_2 and is 1.14 V at standard pressure and 200°C for the gas reaction. When no current is drawn, the open circuit voltage is 1.1 V in $LaPO_4$, which is very close to the theoretical value. Due to the partial short circuit, $CePO_4$ has an open circuit voltage of 0.3 V (both OCV measurements from private communication with H. L. Ray), which is significantly less than the theoretical potential and that from $LaPO_4$. Thus, it seems that while there is significant electronic conductivity causing a partial short circuit in $CePO_4$, some protons are still transported through the electrolyte to create a small OCV.

Rare–earth phosphates hold much promise for applications that require high proton conductivity, but fundamental parameters affecting the conductivity are still difficult to engineer in part due to a lack of atomic scale understanding. In particular, conductivity is controlled mainly by the activation energy barrier for proton transport and the proton concentration. Most experimental measurements such as AC impedance spectroscopy can only access bulk properties of these materials, so an in–depth understanding demands first–principles calculations. In the next section, the parameters controlling ionic and polaronic conductivity will be presented and the method for modeling transport at the atomic scale will be discussed.

1.2 Background

1.2.1 Ionic and polaronic conductivity

Conductivity, σ, depends on the charge of the ion (z), the electric charge of an electron (e), the number density (n) and the drift mobility (μ), such that

$$\sigma = z * e * n * \mu. \tag{1.2}$$

Ionic transport often occurs in a series of rare events, where the ion mostly oscillates in a global or local energy well with energy barriers greater than its thermal energy. Once in a while the ion will hop to another energy minima. Thus, the mobility is temperature dependent and exponentially related to the activation energy barrier for transport, E_a, in the Nernst–Einstein relationship

$$\mu = \frac{e}{kT} D = \frac{e}{kT} \frac{a^2 \Gamma}{2} \tag{1.3}$$

where again, e is the carrier charge,
D is the self–diffusion coefficient, which assumes the correlation factor is unity,
a is the jump distance,
Γ is the jump rate (sometimes defined as τ),
k is Boltzmann's constant,and
T is the temperature in Kelvin.

The jump rate depends on the attempt frequency, τ_0, and the minimum activation energy barrier for transport through the material, such that

$$\Gamma = \tau_0 * d * \exp\left(\frac{-E_a}{kT}\right) \tag{1.4}$$

where d is the number of nearest minima to which the ion can hop.

The parameters that determine conductivity can be investigated both experimentally and with simulation. Let us start by looking at how to control the proton concentration experimentally. Protons are introduced into the rare–earth phosphates by aliovalent doping, which can be understood through defect chemistry. While there are a number of methods to synthesize these doped phosphates, one of the most straightforward is to mechanically mix SrP_2O_7 and $LaPO_4$ and then sinter at high temperature. In the Kröger–Vink notation this is

$$2\mathrm{SrP_2O_7} + 2\mathrm{LaPO_4} \xrightarrow{\mathrm{LaPO_4}} 2\mathrm{Sr'_{La}PO_4} + \mathrm{P_2O_7}{}^{\bullet\bullet}_{\mathrm{2PO_4}} \tag{1.5}$$

such that two aliovalent Sr dopants charge compensate for the effective double positive charge of one pyrophosphate defect. This pyrophosphate defect is an oxygen vacancy where two phosphate tetrahedra rotate in order to share an oxygen (Figure 1). The Sr_{La}' is often thought of as a negative point defect that traps positive defects, such as pyrophosphates [11] or protons, in a deep potential energy well. There is much debate over the extent of the potential well created by the effective negative defect in the literature, which is explored in Chapter 2.

The maximum concentration of protons in $LaPO_4$ is determined by the solubility limit of Sr and the balance between the pyrophosphate and proton concentrations. STEM–EDAX measurements of element concentrations shows that other impurities are not found and a calculation on the similar material, $\mathrm{LaNbO_4}$, shows that La vacancies have a Frenkel defect formation energy of 7.45 eV and are thus unlikely[12]. Thus in the bulk,it is expected that the dominant charged defects are pyrophosphates, protons, holes and aliovalent dopants.

In $\mathrm{CePO_4}$, on the other hand, electronic conductivity with positive carriers has been observed[8]. The authors in Ref. [8] assume that the carrier is a hole sitting on the Ce ion to create $\mathrm{Ce^{4+}}$ in oxidizing conditions, as follows:

$$2\mathrm{Sr}'_{\mathrm{Ce}} + 2\mathrm{Ce}_{\mathrm{Ce}} + \mathrm{P_2O_7}{}^{\bullet\bullet}_{2\mathrm{PO_4}} + \tfrac{1}{2}\mathrm{O_2} \xrightarrow{\mathrm{CePO_4}} 2\mathrm{Sr}'_{\mathrm{Ce}} + 2\mathrm{Ce}^{\bullet}_{\mathrm{Ce}} + 2\mathrm{PO_4}{}_{\mathrm{PO_4}}. \tag{1.6}$$

The nature of the hole (if it is a small polaron localized on a $\mathrm{Ce^{4+}}$ ion) is the subject of Chapter 3. The balance between protons and holes is important information for understanding mixed conductivity in $\mathrm{CePO_4}$ in fuel cell conditions, where there is a reducing atmosphere on one side of the electrolyte and an oxidizing atmosphere on the other.

In wet reducing conditions, water can fill the pyrophosphate oxygen vacancy and introduce protons

$$2\mathrm{Sr}'_{\mathrm{Ce}} + \mathrm{P_2O_7}{}^{\bullet\bullet}_{2\mathrm{PO_4}} + \mathrm{H_2O} \xrightarrow{\mathrm{CePO_4}} 2\mathrm{Sr}'_{\mathrm{Ce}} + 2\mathrm{HPO_4}{}^{\bullet}_{\mathrm{PO_4}} \tag{1.7}$$

which charge compensate for the aliovalent dopant. This equation also describes how protons are incorporated in $\mathrm{LaPO_4}$ (substitute all Ce cations with La) as in Figure 2.

First–principles thermodynamic calculations can compare the energy of formation of these different defects and thus predict their concentrations at various environmental conditions (such as oxygen pressure and temperature). These types of calculations are presented in the work by Solomon et al. for $\mathrm{LaPO_4}$ [11]. In addition, first principles calculations can determine the minimum energy path (MEP) and E_a for ionic transport using transition–state theory (TST). The next subsection presents the bare–bones of density functional theory, which is used in this work to calculate ionic conductivity parameters from first–principles.

1.2.2 First Principles Calculations

Density function theory (DFT) calculations offer the optimal balance between computational expense and accuracy for calculating the properties of extended crystals and is the powerhouse first–principles tool for materials science. While coupled cluster calculations are more accurate, feasible calculations are limited to small molecules, and application to systems with large nuclei such as the lathanides are difficult. Calculation of defects in crystals (with experimentally accessible concentrations) or grain boundaries and surfaces demand supercells with more atoms than can be handled with the coupled cluster method. For example, to simulate 3% Sr–doped $LaPO_4$ demands at 2x2x2 supercell with 196 atoms.

DFT is a variational method that finds zero temperature ground state energies and electronic structure for condensed matter. Finite–temperature calculations are possible using harmonic vibrational theories for solids, or ab–initio molecular dynamics, although these calculations are considerably more computationally demanding than a zero–temperature energy calculation. Often empirical potentials are used for molecular dynamics calculations, such that 100,000s of atoms and long times scales reaching nanosecond lengths can be simulated [13]. MD and kinetic Monte Carlo (KMC) calculations are ideal for calculating diffusivities of ions, but diffusivities can also be estimated from ground–state DFT calculations using transition state theory (TST) as will be described below.

Density functional theory has been very well documented [14], and only a brief summary will be provided here.

Hohenberg and Kohn showed that the total energy of a system and all other ground state properties are functionals of and depend solely on the distribution of the system's particle density[15]. Thus one can vary the electron charge density until the lowest energy distribution is found and this is the ground state energy of the system. The energy of a condensed matter system depends on the kinetic energy $T[n]$ and interaction energy of the electrons $E_{int}[n]$, an external potential, $V_{ext}(\mathbf{r})$, and the Coulomb energy of the nuclei E_{II} as below:

$$E[n] = T[n] + E_{int}[n] + \int d^3r V_{ext}(\mathbf{r})n(\mathbf{r}) + E_{II}. \tag{1.8}$$

For a given external potential, there exists one ground state electron density, $n_0(\mathbf{r})$, which gives the lowest energy solution, $E[n_0]$, to the full many-body Hamiltonian. Furthermore, the Hohenberg-Kohn Theorem also states that the external potential in equation (1.8) is determined uniquely by the ground state density, $n_0(\mathbf{r})$, within a constant. This relationship is fundamental in self–consistently solving for the ground–state solution to the system's Hamiltonian. But first let us tackle some of the vocabulary of DFT, where most of the formalism presented here is inspired from Richard Martin's comprehensive book, Electronic Structure: Basic Theory and Practical Methods [14].

What is a density functional? A functional takes functions, for example the electronic charge density (which is a function of position), as input and outputs a scalar number, such as the energy. Unfortunately, the exact form of the functional that gives the energy from the charge density is only known for the hydrogen atom and the barrier to the exact solution is the many–body problem of interacting electrons. Thus, the exchange and correlation between electrons must be estimated and in the quasi–particle formalism developed by Kohn and Sham[16], these contributions give rise to an extra potential felt by the electrons. It turns out that the exact solution for the exchange and correlation energy of a homogeneous electron gas can be calculated by QMC, so this functional is used in the local density approximation (LDA).

At each point in the computational cell, $\mathbf{r}$, the exchange–correlation energy is taken from that of a homogeneous electron gas with the same density as is found at that point, in the LDA. Since the LDA was implemented, there have been many improvements to take into account non–local effects, such as the generalized gradient approximation (GGA)[17]. In GGA the gradient of the density factors into the energy functional, but there is no one way to implement the gradient, leading to a multitude of GGA functionals.

The general scheme for minimizing the energy is an iterative process of solving the eigen–equation for the energy and wavefunctions using the system's Kohn–Sham Hamiltonian, both given below

$$(H^\sigma - \varepsilon_i^\sigma)\psi_i^\sigma(\mathbf{r}) = 0 \tag{1.9}$$

$$H^\sigma(\mathbf{r}) = -\tfrac{1}{2}\nabla^2 + V_{\text{ext}}(\mathbf{r}) + V_{\text{Hartree}}(\mathbf{r}) + V_{\text{xc}}(\mathbf{r}) \tag{1.10}$$

where the Hartree energy would be $E_{\text{Hartree}}[n] = \frac{1}{2}\int d^3r d^3r' \frac{n(\mathbf{r})n(\mathbf{r}')}{|\mathbf{r}-\mathbf{r}'|}$ and the exchange–correlation potential, $V_{\text{xc}}(\mathbf{r})$ is taken from either LDA or GGA functionals.

The initial charge density is guessed, often by superimposing the densities of free atoms, or the initial wavefunctions are estimated. They are related by:

$$n(\mathbf{r}) = \sum_{i=1}^{N} |\psi_i(\mathbf{r})|^2 \tag{1.11}$$

where the sum over wavefunctions in (1.11) does not explicitly take spin into account.

For a given external potential and initial electron charge density, the Hamiltonian can be solved for the eigenvalues and vectors (energy and wavefunctions). Convergence to the ground state is reached when the initial energy does not differ more than the given tolerance from the final energy. If convergence is not reached, the new wavefunctions are created, often by mixing the initial wavefunctions, and used to initialize the next self–consistent step with $n_0(\mathbf{r})$.

$$\begin{tikzcd} n_0(\mathbf{r}) \arrow[r] & V(\mathbf{r}) \arrow[d] \\ \psi_0(\mathbf{r}) \arrow[u] & \psi_i(\mathbf{r}) \arrow[l] \end{tikzcd} \tag{1.12}$$

This process has been widely successful in predicting the electronic structure of condensed matter, but has also failed in many ways such as predicting a metallic NiO[18] due to its inability to describe the ‘d’–electrons in Ni. Highly localized electrons or holes suffer from a large self–interaction error which is not completely corrected by the local density approximation or GGA.

For example, ‘d’– and ‘f’–electrons end up “seeing” themselves through the density at their point in space and want to delocalize to decrease their potential energy. Significant improvements to the exchange and correlation potential given by LDA and GGA come at a high computational cost. For example, researchers can use hybrid functionals which add a percentage, usually 25%, of Hartree–Fock exact–exchange into the Hamiltonian, but this significantly increases the required computational time[19]. While this method has been shown to be sufficient in many studies (for example in iron oxides and ceria [20, 21, 22]), the percentage of exact exchange to use is not theoretically specified and it does not directly address the need for an improved description of the correlation energy. A cheaper method, DFT plus a correction based on a Hubbard-model term, has been utilized since the early 1990s [23], which creates a penalty on specific orbitals for partially occupation due to delocalization from the self–interaction error.

Discussion of the Hubbard–U parameters in the context of $CePO_4$ can be found in Chapter 2. The appropriateness of using the DFT+U approach to model polaron transport is discussed in Chapter 3.

1.2.3 NEB and modeling polarons

As indicated above, transition state theory states there is a minimum energy path for a reaction and this can be determined within DFT using the nudged elastic band (NEB) method or the climbing image NEB[24]. This method has been successfully employed to calculate the activation energy for proton transport through $LaPO_4$ [9] and matches experiment remarkably well.

Transition state theory applies to activated processes, where the reactants start in a potential well and move over a saddle point to another potential energy well to become the products. In order to use this method, global or local minima in the potential energy landscape must be known. If the reactant state is known, there are methods that can search for the product state[25], but for describing proton and polaron transport it is easy enough to guess and then search for the energy minima. For example, in Yu and De Jonghe's [9]work on proton transport in $LaPO_4$, a fine mesh was created in the unit cell and the protons placed at the mesh's lattice points were relaxed to find the minima.

Once the reactant (initial) and product (final) states are known, a series of images are created along the reaction coordinate. The reaction coordinate is actually a multidimensional coordinate that captures of all the ion and electron motion from the initial and final states. The initial state is often set to 0 and the final state to 1, as in Figure 4.2.

Finding the saddle point is the major endeavor of NEB; since density functional theory is designed to find energy minima, additional constraints must be employed to find the saddle point and images along the path. The saddle point is defined as a point of positive curvature in all directions but one. The negative curvature in one direction at the saddle point can be confirmed by the imaginary mode in the DFT calculation of the phonon spectrum (Chapter 4). While most of this thesis is not concerned with NEB calculations, I will offer a brief explanation since calculating the activation energy from the saddle point is a major component of predicting conductivity in Chapter 4.

In order to keep the saddle point or any of the images created along the reaction coordinate from falling back into the minima, the images are attached by an elastic band (a spring), such that the image is pushed away from its nearest neighbor images if it gets too close. These images can also wander away from the minimum energy path, so the spring also pulls the images together if they move too far apart.

In a standard minimization calculation, the force on each ion is calculated and the ion is moved a pre–specified distance in the direction of the force. In the NEB method, the forces on the ions are modified by a spring constant to 1) keep the images from relaxing into the minima and 2) to keep the images along the path. The NEB method is well described in the literature, but the main equations are provided here to help orient the reader. The following equations show the modified forces:

$$F_i = -\nabla E(r_i) \tag{1.13}$$

$$F_i^{\perp} = F_i - (F_i \bullet \hat{\tau})\hat{\tau} = 0 \tag{1.14}$$

$$F_{i,\text{update}} = F_i^{\perp} + F_{i,\text{spring}}^{||} \tag{1.15}$$

$$F_{i,\text{spring}} = K(|r_{i+1} - r_i| - |r_i - r_{i-1}|) \tag{1.16}$$

$$F_{i,\text{spring}}^{||} = (F_{i,\text{spring}} \bullet \hat{\tau})\hat{\tau}. \tag{1.17}$$

In these equations, F_i is the Hellmann–Feynman force on an ion in image i. $\hat{\tau}$ is the unit vector that points between image i and image $i+1$. The parallel component of the force projected along $\hat{\tau}$ would pull the image into the potential well, so only the perpendicular component of the force is used to move the ions. The spring force keeps the images well spaced. Only the parallel component projected on $\hat{\tau}$ that keeps the images closer to the transition point rather than the minima is used to update the ion positions.

The NEB method works well for ionic transport, but has not been used to model polarons. In particular, small polarons with a highly localized electron or hole and lattice distortion smaller than the unit cell size should hop similarly to protons or other small ions. Thus, the saddle point for hopping needs to be determined in order to find the activation energy. The nudged elastic band method is not always necessary if the transition point is very symmetric. Then using a force–based ion relaxation method rather than the conjugate gradient method that finds minimum energy solutions, one can find the zero–force saddle point. It is possible that the NEB can work for finding the MEP of polaron transport, but the literature remains sparse. One cannot calculate a Hellmann–Feynman force on the electron or hole–polaron and update its position. Instead only the polarization of the lattice can be modified. Modeling polaron transport in condensed matter remains a rich field of exploration.

The main body of this dissertation is organized as follows: first proton–dopant interactions in $LaPO_4$ are presented, second the electronic structure of $CePO_4$ and potential for small polaron formation on the Ce ions is discussed, and finally a new method for modeling small polaron transport in solid state electrolytes is explained. Combining the knowledge of these three chapters allows researchers to address mixed conductivity in rare–earth phosphates – a course of future work.

Chapter 2

Proton-Ba Interactions in Doped $LaPO_4$[1]

The interactions between an aliovalent cation dopant, Ba, and protons in $LaPO_4$ are studied with first-principles density functional theory. This work is motivated by the desire to use doped $LaPO_4$ as a proton conducting solid electrolyte or hydrogen separation membrane. In this context, the strength and range of proton-dopant interactions are important factors underlying proton mobilities. Using periodic supercells, we find that 3% Ba-doping stabilizes a proton at a distance 2.7 Å from the dopant by up to 0.2 eV relative to positions far from the dopant. The Ba-dopant creates a narrow potential energy well and only changes the proton's potential energy surface by ±0.05 eV when the proton is farther than 2.7 Å from the dopant. Electrostatic interactions between the proton and dopant account for the majority of the binding energy of proton sites and are associated with a complex redistribution of the charge induced by the dopant on the neighboring oxygen ions. In contrast, the strain field created by the Ba-dopant gives rise to a relatively small contribution to the interaction energy.

2.1 Introduction

Rare-earth phosphates are attractive candidates for electrolytes in intermediate-temperature fuel cells, or in hydrogen separation membranes and sensors. The impact of aliovalent doping on proton conductivity in rare-earth phosphates has been explored experimentally in a

---

[1] This work was previously published in the Journal of Materials Chemistry as: N. Adelstein, J. B. Neaton, M. Asta, and L. C. De Jonghe. First-principles studies of proton-Ba interactions in doped $LaPO_4$ *JMC.* DOI: 10.1039/c2jm16214h (2012).

number of recent studies[26, 27, 28, 29, 2]. In particular, lanthanum orthophosphate and metaphosphate compounds doped with calcium, strontium, and barium have been shown to be proton conductors that are relatively stable under humid conditions and up to high temperatures. However, an order of magnitude increase in the conductivity of the protons is still required in these compounds for technological applications. Aliovalent doping is required for proton incorporation, but a strong attraction between the dopant and proton can impede conduction. Here we focus on the binding energies between protons and aliovalent alkaline-earth cation dopants in $LaPO_4$ and the dopant's effect on proton conductivity in this compound, as an important step towards understanding how this property can be optimized.

When a divalent alkaline-earth (AE) ion substitutes for a trivalent rare-earth (RE) ion in the RE-phosphates, the result is an effective negative charge, e.g., a $\mathrm{Ba'}_{\mathrm{La}}$ defect in Kröger-Vink notation. This effective negative charge is expected to lead to an electrostatic attraction for the positively charged protons, causing them to reside in the vicinity of the AE dopant. Such an attractive interaction between protons and dopants in La-based metaphosphate glasses doped with aliovalent AE elements was observed in recent vibrational spectroscopy measurements by Harley et al. [30] and using 1H{137Ba} TRANsfer of Populations in Double Resonance (TRAPDOR) NMR experiments[31]. Significant differences in the conductivity of polycrystalline $LaPO_4$ due to 1% doping with Mg, Ca, Sr, and Ba, has been measured experimentally[27]. Ba^{2+} is the largest of the experimentally tested dopants at 1.21 times larger than La^{3+} and shows a lower conductivity than samples doped with Ca and Sr in the above study. The lower conductivity of the Ba doped sample is explained by its lower solubility of 0.4% (compared to the 1.9% solubility of Sr), though each sample is nominally 1% doped.

It has been debated in the literature whether aliovalent dopants trap protons due to electrostatic interactions and thus increase the activation energy barrier for transport [32, 12, 33]. While experimental evidence has been sought for trapping in rare-earth phosphates [30], we are unaware of previous computational studies directly investigating the nature of proton-dopant interactions in these systems. The magnitude and origins of the interactions between protons and aliovalent dopants has been widely studied in proton conducting perovskites (ABO_3)[34, 35, 4]. For example, in a DFT study by Björketun, et al. on aliovalently doped $BaZrO_3$, it was found that the proton is stabilized by more than 0.15 eV when bound to the dopant's nearest oxygen neighbors[36]. Similar results were also obtained in the same system in a computational study employing classical interatomic potentials[33]. Experimentally, NMR (spin-echo) confirms that the proton preferentially sits near the dopant in $BaZrO_3$[37].

Previous first-principles calculations of protons in $LaPO_4$ by Yu and De Jonghe[9] determined low energy binding sites and predicted the activation energy for proton transport to be 0.8 eV; the effect of dopants was not considered in this study which made use of a

Table 2.1: Example lattice parameters from site 8 (see Figure 1) for undoped (bulk) and doped $LaPO_4$ computed in the present work using a 2x2x2 supercell are compared with experiment. The lattice vectors are given in Å while the angles are in degrees.

Lattice parameters	Experiment	Bulk calc.	H^+LaPO_4	$BaHLaPO_4$
a	6.8313	6.94	6.92	6.95
b	7.0705	7.15	7.14	6.95
c	6.5034	6.54	6.54	6.95
α	90	90	89.9	89.9
β	103.27	103.77	103.69	103.73
γ	90	90	90.3	90.3

homogeneous negative background charge to compensate the positive charge of the proton. The presence of aliovalent dopants will cause a wider range of activation energy barriers for proton hopping. Evidence for changes in activation barriers upon doping was obtained from the recent AC impedance spectroscopy measurements of doped metaphosphate glasses by Harley and De Jonghe[38]. The spread of activation energies due to the dopant was concluded by Harley and De Jonghe to correlate with a decreased conductivity in the metaphosphate glasses.

As in proton-conducting perovskites[39], the minima in the proton's potential energy surface corresponds to environments where the proton bonds to an oxygen, creating a hydroxyl bond, and participates in hydrogen bonding with a neighboring oxygen ion[9]. In the current study we compare twenty such binding sites in 2x2x2 supercells, eight of which are isoenergetic in the undoped cell and significantly more stable than the other twelve sites. We find that the interaction between the dopant and proton is attractive at very short distances and varies non-monotonically with distance. We analyze the origins of this behavior by examining in detail the change in electronic structure and ion displacements that determine the relative energetics of the different proton binding sites. A multistep procedure, similar to that employed in Ref. [36] and an earlier study on CeO_2[40], is used to assess the relative importance of electrostatic versus strain effects, as will be described in the next section.

2.2 Computational Methods

All DFT calculations are performed within the generalized gradient approximation (GGA) of Perdew, Burke, and Ernzerhof (PBE)[17]. The VASP code[41, 42] and the projector augmented-wave (PAW) method[43] are used for all calculations. The PAW potentials use 11 valence electrons for La ($5s^25p^66s^25d^1$), 10 for Ba ($5s^25p^66s^2$), 5 for P ($3s^23p^3$), and 6 for O ($2s^22p^4$). A plane-wave energy cutoff of 500 eV is used for the expansion of the electronic wave functions. A Monkhorst-Pack[44] grid of 2x2x2 is employed in the integrations over the Brillouin zone of the supercells (which are 2x2x2 periodic repetitions of the basic unit cell in real space, see below). Total energies are converged to 10^{-6} eV and Hellmann-Feynman forces on the ions are converged to 50 meV/Å.

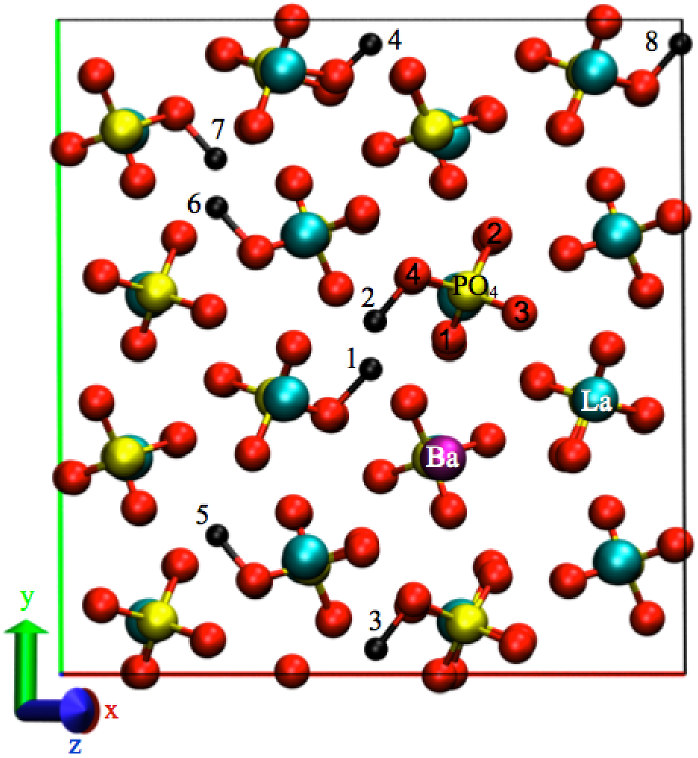

Figure 2.1: The 2x2x2 doped $LaPO_4$ supercell employed in the present calculations is shown projected along a $[10\bar{1}]$ direction. The Ba dopant is shown in purple and the La cations in blue. The phosphate tetrahedra are made of four red oxygen ions covalently bonded to a yellow phosphorus. The black proton's eight degenerate global energy minima in the bulk $LaPO_4$ crystal are numbered 1-8 in order of their distance from the dopant.

At room temperature, crystalline $LaPO_4$ has the monoclinic $P2_1/n$ structure with 4 formula units per primitive cell and all atoms sitting in 4e Wyckoff positions[7]. To model doped systems, 192-atom supercells are constructed by doubling the primitive cell along each of the lattice vectors. Our computed lattice parameters for a characteristic supercell containing a proton and Ba cation dopant are given in Table 2.1. Our results for the undoped $LaPO_4$ structure compare well with previous calculations by Yu and De Jonghe[9] and experiment. Upon addition of the proton using a uniform negative background charge, the unit cell volume decreases less than 0.5% and upon addition of the Ba dopant, the unit cell volume increases by on average 0.7% compared to the bulk.

Since the inhomogeneity of the potential energy surface can obscure the effect of the dopant on the total energy of the cell, we will determine the nature of the interaction between Ba dopants and protons by comparing energies as a function of distance for protons in sites corresponding to the global energy minimum positions in the undoped supercell. These sites were identified in previous calculations of the potential energy surface for protons in $LaPO_4$[9]. Local minima were also calculated and are about 0.4 eV higher in energy than the global minima, as shown in Figure 2.2.

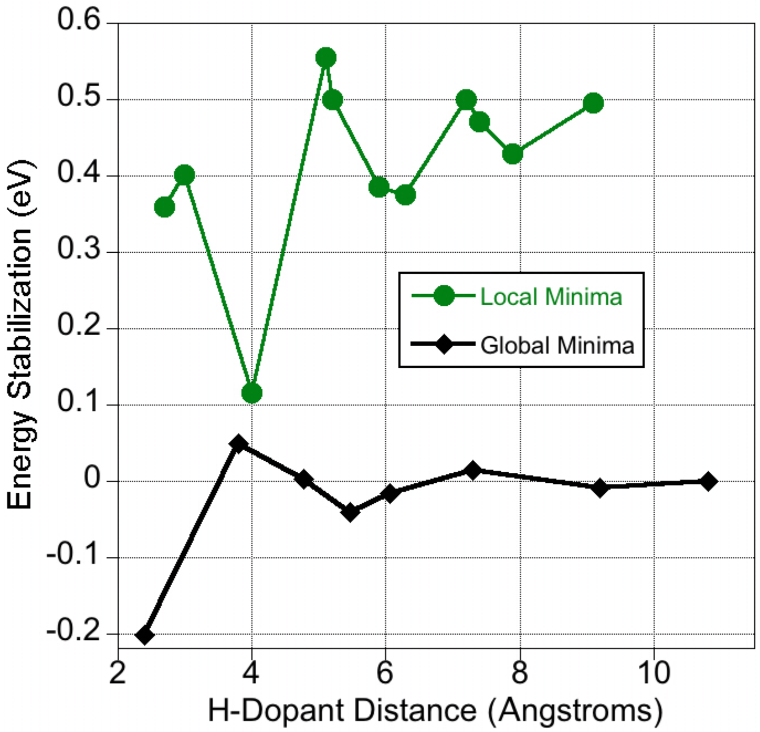

Figure 2.2: Then energy versus proton-dopant distance for the global and local minima show that the global minima are about 0.4 eV lower in energy.

The proton's binding site depends not only on which of the four distinct oxygen ions creates the hydroxyl bond, but also which other oxygen ion is involved in hydrogen bonding with the proton. Thus, the orientation of the hydroxyl bond also needs to be determined for each of the proton binding sites. To illustrate the complexity of the energy surface, consider the proton in a hydroxyl bond with oxygen 4 as labeled in 2.1. The proton could form a hydrogen bond with eight neighboring oxygen ions of the following types and distances (in parenthesis) from the O4 hydroxyl oxygen: O1 (2.86, 2.87, 3.01 Å), O2 (2.85, 2.92, 3.37 Å), and O3 (2.92 Å). By placing the proton near O4 and optimizing its position with DFT, we find the minimum energy hydrogen bond to be with the O1 (3.01 Å) oxygen, where the oxygen-oxygen distances are taken from the undoped cell, as shown in Fig 2.1. Upon addition of the proton, the O4-O1 oxygen distance decreases to 2.5 Å in order to accomodate hydroxyl and hydrogen bond lengths of 1.0 and 1.5 Å, respectively. The O4 ion differs from the other three oxygen-ions in having the shortest phosphorous-oxygen bond length (1.53 Å compared to 1.57 Å for the other three oxygen-phosphorous bonds).

Substituting a single Ba dopant for a La cation necessarily breaks the symmetry of the crystal and causes variations in the energy of the proton in sites that are isoenergetic in the undoped cell. Figure 2.1 shows a projection of the 2x2x2 supercell used in the present calculations and illustrates how the distance and orientation of the proton relative to the Ba'$_{\mathrm{La}}$ defect and neighboring oxygen ions differs for each of the eight sites considered in this study (each of which corresponds to the global energy minima in the undoped $LaPO_4$ crystal). To explore the impact of the proton's proximity to the Ba dopant on the binding energy we compare the differences in the total energy of supercells with the proton relaxed at each of these eight sites. Amongst these sites, the largest distance between a proton and the dopant is roughly 11 Å (labeled site '8' in Figure 2.1). To ensure that the introduction of the dopant does not lead to the formation of other low-energy sites for the proton, we explored an additional 12 local-minimum geometries involving binding of the proton to different oxygen ions, and found that on average they are 0.4 eV higher in energy than the sites shown in Figure 2.1.

We use a 2x2x2 supercell with one La replaced by Ba. This gives a dopant concentration of 1/32, or approximately 3%. We note that this concentration is significantly larger than the solubility limit of 0.4% reported experimentally for Ba in $LaPO_4$[27]. However, the results presented below show that the dominant interactions between the proton and dopant occur at relatively short separation distances, below approximately 6 Å. Thus, the results indicate that the 2x2x2 supercell employed in this work is large enough to avoid significant spurious interactions between the proton and the periodic images of the dopant, and that the results presented below correspond to dopant-proton interaction in the limit of the dilute dopant concentrations relevant to the experimental measurements.

2.3 Results and Discussion

Figure 2.3 plots the total energy of the system as a function of the distance of the proton from the Ba dopant (the proton sites are labeled 1-8 with increasing distance from the Ba). In this plot, the energy reference corresponds to a proton at the site furthest from the dopant in the supercell (site 8) and negative energies correspond to attractive interactions with the dopant relative to the reference, while positive values are repulsive.

The main results in Figure 2.3 can be summarized as follows. The most stable binding site for the proton is found on the oxygen ion closest to the dopant. When the proton is at this site, the energy of the system is 0.2 eV lower than when the proton is furthest away from the dopant. As the distance of the proton from the dopant increases, the energy is seen to vary non-monotonically and features the peak repulsive interaction energy with a proton-Ba distance of 3.9 Å at site 2, i.e. the second closest site. In the following sections we discuss the relative importance of the electrostatic and elastic interactions between the proton and the dopant and how these interactions give rise to the distance dependent binding energies plotted in Figure 2.3.

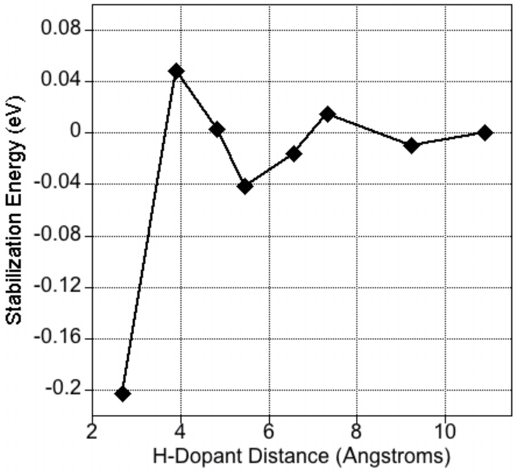

Figure 2.3: The stabilization energy of proton sites compared to site 8, with the H-Ba$_{La}$' distance of 10.89 Å, is shown for eight proton sites in the 2x2x2 supercell.

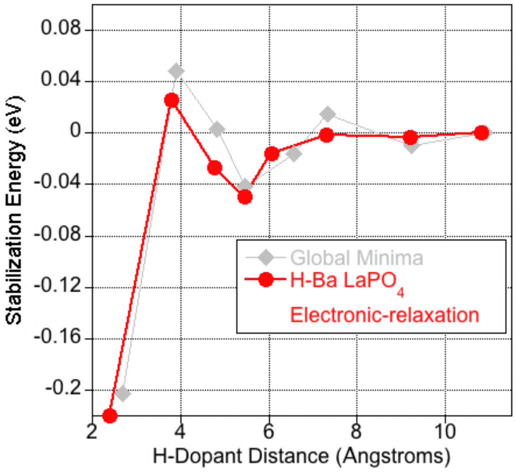

Figure 2.4: The stabilization energy from the electronic relaxation effect closely matches the total stabilization energy after complete optimization.

2.3.1 Electronic Relaxation

The curve labeled "Electronic Relaxation" in Figure 2.4 corresponds to binding energies calculated in the Ba-doped supercell with the ions fixed at their optimized positions in the supercell with just the proton. Thus these binding energies arise solely from electronic redistribution induced by adding the Ba dopant. For comparison, the grey points in Figure 2.4 are identical to the data in Figure 2.3, and correspond to energies derived allowing full relaxation of the ion positions. It can be seen that the electronic relaxation results are very close in energy to those derived from calculations allowing full ionic relaxations. This indicates that strain-induced interactions are relatively small, as will be discussed in more detail in the next section.

When just considering the electronic relaxation effect, the second closest proton site, 3.8 Å away from the dopant, is the only site with a (slightly) higher energy than the site furthest from the dopant (i.e., site 8). The third through fifth closest sites show slightly lower energies relative to site 8, with the fourth closest site showing some enhanced stabilization. The energy variation with proton distance is negligible beyond site 5.

To understand the non-monotonic dependence of the energy on the proton-dopant separation, we examine the charge redistribution due to the dopant and compare the environment around each proton. In particular, we will focus on sites 1, 2 and 4 as labeled in Figure 2.1. The charge redistribution plotted in Figure 2.5 is defined as the charge density difference for the two systems, one with and one without the dopant, holding all ions fixed. La nominally donates 3 valence electrons to its surrounding 9-oxygen shell, while the aliovalent Ba dopant and hydrogen atom together nominally donate 3 electrons, which would create an effective negative charge near the Ba^{2+} dopant. By comparing the charge density difference for each proton site 1-8, we find that the oxygen-shell around the dopant contains essentially the same number of electrons independent of proton position, so we only show the charge density difference for site 2 with proton positions 1 and 4 superimposed. Moreover, we find that the Ba dopant induces areas of significant electron charge density accumulation and electron charge density depletion around the nearest and next nearest neighbor oxygen shell. Thus, it is unsurprising that the protons potential energy surface near the Ba dopant does not exhibit a simple Coulombic potential well.

Figure 2.5 illustrates layers of charge depletion (green-blue) followed by charge accumulation (yellow-red) around the dopant's 9-oxygen coordination shell. Immediately surrounding the Ba dopant there is a sphere of charge depletion because in La the valence electrons are closer to the core than in Ba. Further out near the 9-oxygen shell, the diffuse area of charge depletion (green crescents) can be explained by the decreased attractiveness of the Ba nucleus versus the La nucleus to the oxygen electrons.

From this analysis, we find that increased proton stability is correlated with the polarization of the oxygen ions involved in the hydroxyl and hydrogen bonds with the proton, and not simply the accumulation of electron density in the immediate vicinity of the proton. While there is no increased charge density exactly at proton site 1, the polarization of the two oxygen ions involved in hydroxyl and hydrogen bonding with the proton (bonds are indicated in Fig 4 (b)) correlates with the 0.22 eV stabilization of the energy relative to site 8. These two oxygen ions are part of the 9-oxygen coordination shell around the dopant, which all show polarization due to the Ba dopant (Fig 4 (b) and (d)).

Oxygen ions further out from the dopant also are polarized, which affects the stabilization

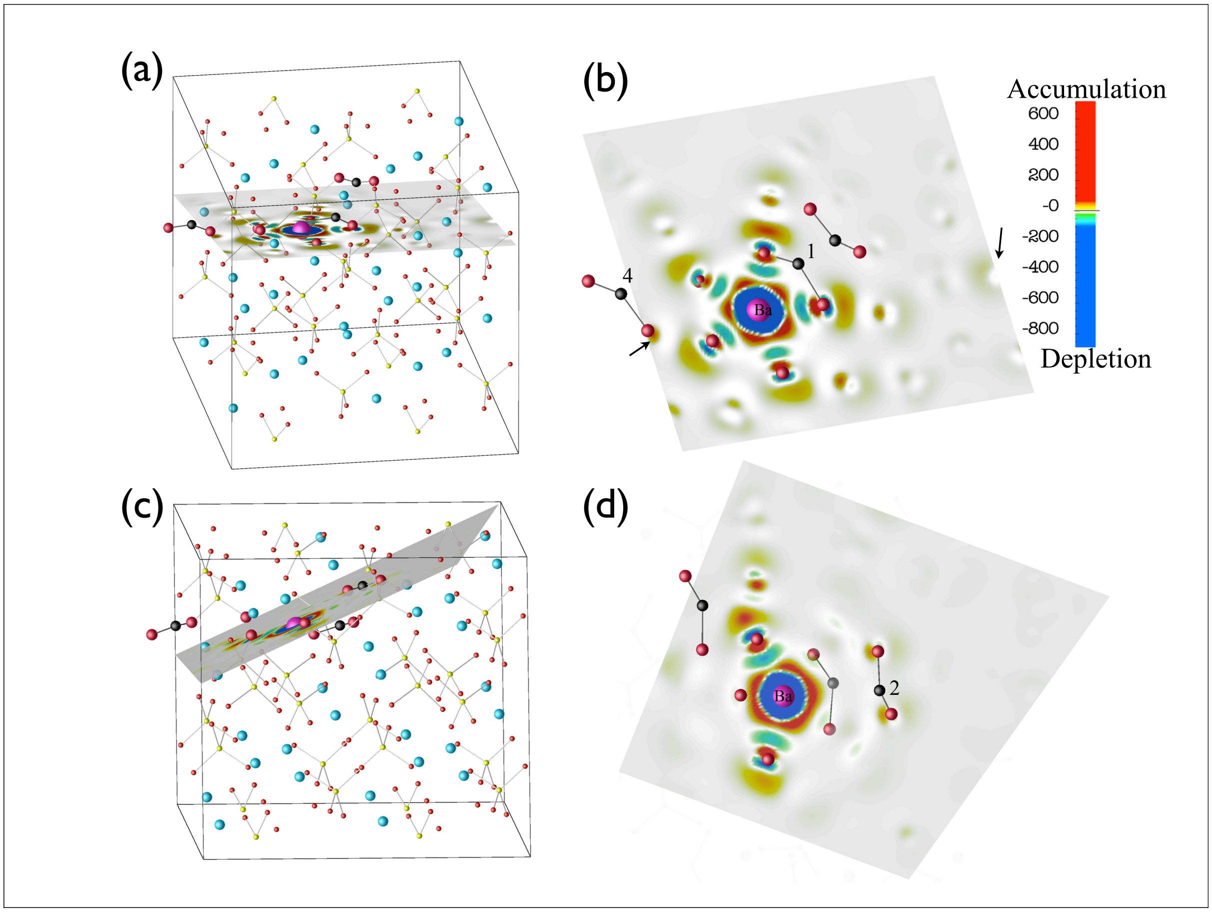

Figure 2.5: The charge accumulation and depletion due to the dopant when the proton is at site 2 is visualized by subtracting the charge density with the H and Ba doped $LaPO_4$ ($\rho_{Ba,H}$) from the charge density with just the proton (ρ_{H^+}). Two volume slices of the charge density difference in the supercell, (a) and (c), are shown face-on with only selected atoms in (b) and (d). The color scheme for the ions is the same as Fig 2.1 and the Ba is labeled for clarity. Proton sites are labeled in order of their proximity to the dopant and positions 1, 2, and 4 are highlighted. The key in the top right hand corner shows that the gray color indicates no difference in the charge density after the dopant is included. Green and blue indicates charge depletion and yellow to red indicates charge accumulation. The volume slice shown in (a) cuts through the oxygen involved in hydrogen and hydroxyl bonds with protons 1 and 4 (which are superimposed on the site 2 charge density difference), while the volume slice in (c) cuts through the oxygen bonding with proton 2.

energy of other proton sites. For example, the proton in site 4 is stabilized by 0.03 eV due to the polarization of the oxygen ions involved in a hydrogen bond with the proton, as shown by the small arrows in Figure 4 (b). In contrast, the proton at site 2 is destabilized 0.03 eV relative to site 8. To illustrate, the volume slice in Fig 4 (c) that contains the oxygen ions involved in hydrogen and hydroxyl bonds with the proton and the Ba dopant in site 2 is shown in Fig 4 (d). The plot indicates that these oxygen ions are not significantly polarized. The polarization of the oxygen involved in hydrogen bonding correlates with the shortening of the hydrogen bond after allowing the ions to relax, such that the hydrogen bond of protons in sites 1 and 4 are the shortest. The changes in bond lengths upon ionic relaxation and the associated changes in binding energy will be discussed in the next section.

2.3.2 Elastic Relaxation

Figure 5 shows the change in proton-dopant interaction energy upon relaxation of the ionic positions. The interaction energy of the proton and dopant increases by at most 0.03 eV (for site 3) (i.e. becomes less attractive) due to ionic relaxation. The data plotted in this figure correspond to the differences between the grey diamonds in Figure 3, derived from the energy of fully relaxed supercells, and the red circles, derived from calculations with fixed ionic positions.

As discussed by Kreuer in his review of proton-conducting perovskites[4], the energy of a proton in a given position can be understood to be governed by a competition between two factors: the energy gain induced by shortening of the hydrogen bond, and an energy penalty associated with shortening the oxygen-oxygen (O-O) neighbor distance, such that these two distances are correlated (Fig 2.7 and Table 2.3). Kreuer's analysis holds well for proton sites 5-8, as shown in Fig 2.6 by the correlation of the hydrogen bond length (black squares) and the strain-mediated interaction energy. We hypothesize there is little strain field overlap between the proton and the dopant for these sites, so the elastic relaxation just depends on the hydrogen bond length and O-O distance. On the other hand, when the proton is closer than 6 Å from the dopant, elastic relaxations lead to a repulsive contribution to the proton-dopant interaction energy independent of the lengthening or shortening of the hydrogen-bond.

The repulsive elastic effect is likely due to additional ion displacements, which are caused by the interaction of the proton and dopants strain fields. Since the Ba dopant is larger than the host La cation, it pushes the oxygen ions in its 9-oxygen shell 0.1-0.2 Å away. Positive displacements of the closest 10 ions to the Ba-dopant from site 8, as shown in Table 2.2, columns 2 (type) and 3 (displacement from ion positions in the undoped supercell), indicate that all the ions have moved away from the Ba. These oxygen ions in sites 5-8 are free to move away from the dopant because they are not constrained by the proton's strain field.

Table 2.2: The displacement of the 10 closest ions around the Ba-dopant (column 2) and proton (column 3) from their ideal positions for site 8 is shown. The average Ba-O bond length for the oxygen ions in the 9-oxygen shell around the dopant is shown in the last column.

10 closest ions:	from Ba	from H	Ave. Ba-O (Å)	
1st	O 0.177	O -0.312	site	
2nd	O 0.190	O -0.167	no Ba	2.600
3rd	O 0.173	O 0.027	1	2.722
4th	O 0.154	O 0.027	2	2.740
5th	O 0.144	O 0.255	3	2.748
6th	O 0.234	O -0.002	4	2.757
7th	O 0.172	O -0.039	5	2.756
8th	O 0.093	O -0.051	6	2.755
9th	O 0.092	O 0.032	7	2.756
10th	P 0.124	O 0.005	8	2.756

Columns 6 and 7 in Table 2 show that in undoped $LaPO_4$, the average La-O distance of the 9 closest oxygen ions to the La is 2.600 Å, and while the average Ba-O distance increases for all 8 sites, sites 1-3 show a smaller expansion.

Due to the anisotropic nature of the crystal structure, the resulting displacement field around the proton is fairly complex, leading to both expansions (+) and contractions (-) in the distances between the protons neighboring ions. The proton in site 8, where there is minimal interaction with the dopants strain field, draws the two closest oxygen ions significantly towards itself and pushes the closest La away, as shown in Table 2, columns 4 and 5, along with the displacements of the other 7 closest ions to the proton.

For sites 1-3, the interaction of the proton and dopants strain fields cause the average Ba-O distance to slightly decrease, as shown in column 4, Table 2.2. The overlap of the proton and dopants strain fields destroys the correlation between the hydrogen-bond length (and O-O distance) and the elastic relaxation and causes the largest elastic relaxation effects.

2.4 Summary

Doping $LaPO_4$ with about 3% barium causes the stabilization of the closest proton binding site to the dopant by 0.2 eV. This binding energy between the proton and dopant is found to be predominantly from an electrostatic interaction. In particular, protons are stable

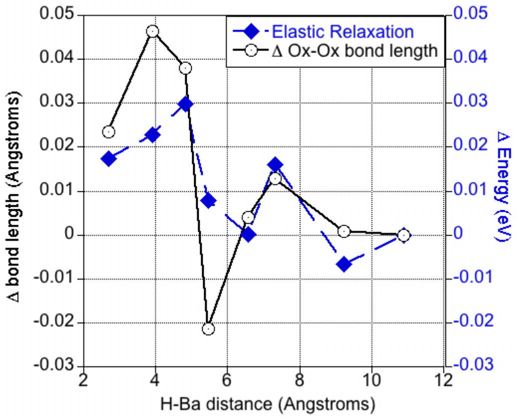

Figure 2.6: The correlation between the hydrogen bond length and the elastic effect is apparent for sites 5-8.

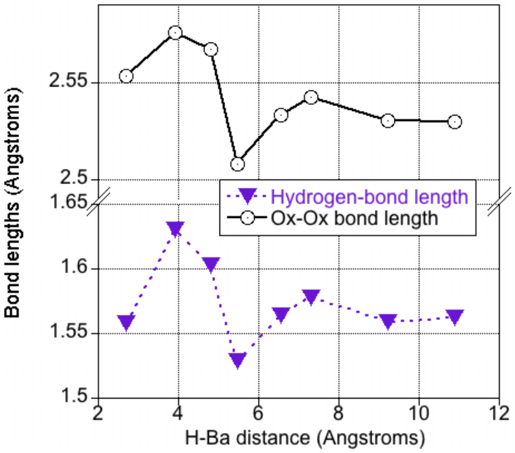

Figure 2.7: The O-O bond length correlates well with the hydrogen-bond length, except for sit 1. The proton draws the two closest oxygen towards itself, decreasing the hydrogen bond and the O-O distance.

when bonded to oxygen ions that are polarized due to the dopant. Much weaker, but non-zero, interactions extend out to distances of approximately 6 Å due to electrostatic and elastically-mediated interactions. While the effect of the dopant is non-local and can be understood in terms of charge redistribution and interacting strain fields, the effective negative charge of the dopant creates a signficant local potential energy well.

The mobility of the proton in the doped $LaPO_4$ crystal will clearly be strongly influenced by the 0.2 eV binding energy near the dopant. The detailed effect of the dopant-proton interaction on mobility ultimately depends on the average energy barrier for hopping between tetrahedra. The minimum energy barrier for the proton to get out of the potential well near the dopant and over site 2 is 0.24 eV and the actual activation energy barrier for motion is most likely significantly higher. Additional calculations of the potential energy surface seen by the proton in different environments show that the energy surface is quite uneven, which is expected to impede proton conduction. It will be beneficial to compare first-principles calculations of Ca and Sr doping in $LaPO_4$ to the experimental measurements, which show higher activation energy barriers than Ba doped $LaPO_4$[27]. Understanding the effect of these different dopants is imperative to engineering better proton conducting membranes.

Table 2.3: The proton stabilization and environment, as described by the hydroxyl and hydrogen bond lengths and the hydroxyl-oxygen hydrogen-oxygen bond lengths (O-O), are given for each site. The effect of the proton on the average Ba-O bond lengths is given in the last column. The last row (0) gives bond lengths without the Ba-dopant and the average La-O bonds.

H^+ site	ΔEnergy (eV)	Hydroxyl bond	Hydrogen bond	O-O bond
1	-0.202	1.035	1.558	2.553
2	0.049	1.025	1.630	2.576
3	0.003	1.027	1.604	2.567
4	-0.042	1.041	1.528	2.508
5	-0.016	1.034	1.564	2.533
6	0.015	1.030	1.577	2.542
7	-0.010	1.035	1.559	2.530
8	0	1.033	1.562	2.529
0		1.03	1.56	2.5

Chapter 3

Structure and electronic properties of cerium orthophosphate: theory and experiment[1]

Using a combination of density functional theory (DFT) calculations and experiments, we determine the structural and electronic properties of cerium orthophosphate ($CePO_4$), a promising proton-conducting electrolyte for fuel cell applications. To better account for strongly-localized Ce $4f$ electrons, we use a DFT + U approach, where the exchange-correlation functional is augmented with an adjustable effective Hubbard-like parameter U. We find that the calculated structural properties are in good agreement with x-ray diffraction measurements, largely independent of the value of U used. However, the electronic structure is much more sensitive to U, and values of U = 2.5-3 eV for Ce $4f$ states provide excellent agreement between the calculated density of states and measured photoemission spectra near the valence-band edge, validating the efficacy of a DFT + U-based approach for this system. With a judicious choice of U determined from photoemission experiments, this work provides a natural starting point for future studies of charge transport and charged defect formation and migration in this important class of compounds.

---

[1] Most of this work was previously published in Physical Review B as: N. Adelstein, B.S. Mun, H. L. Ray, P. N. Ross, J. B. Neaton, and L. C. De Jonghe. Structure and electronic properties of cerium orthophosphate: theory and experiment. *PRB*. 83(20), (2011). Section 3.4.3 is new, as is Table 3.1 and Figures 3.2 and 3.7.

3.1 Introduction

New materials with high proton conductivities in the temperature range 300-500 ° C can be of benefit as solid electrolytes in a variety of electrochemical devices, such as hydrogen sensors, hydrogen separation membranes, and fuel cells. Incorporation of such a material into a fuel cell would, for example, facilitate the in situ reforming of liquid biofuels and reduce the need for noble catalysts. Rare-earth phosphates have been investigated for this purpose because of their stability at high temperatures, and their ability to incorporate protons when doped with aliovalent cations[2, 8, 45, 30].

Recent AC impedance spectroscopy for $CePO_4$ (Ref. [8]) indicates a total conductivity in air an order of magnitude higher than that of $LaPO_4$, a well-known proton conductor. The enhanced conductivity of $CePO_4$ relative to its La-based counterpart has been attributed to hole conduction, based on defect chemistry interpretations of the measured conductivity in both wet versus dry conditions and reducing versus oxidizing environments[8]. First-principles calculations using density functional theory (DFT) can potentially elucidate the differences between $CePO_4$ and $LaPO_4$ conductivities. However, whereas ground-state electronic structure and proton conduction have already been studied with DFT for $LaPO_4$[9] the electronic structure of $CePO_4$ is entirely unexplored. In $CePO_4$, highly localized 'f' electrons can result in strong correlations that affect electronic structure and defect formation.

In this work, we show that the ground-state geometry and electronic structure of $CePO_4$ can be obtained with good accuracy using DFT-based methods via direct comparison to x-ray diffraction measurements and photoemission spectroscopy. We address the impact of the strongly localized Ce $4f$ states with an adjustable effective Hubbard-like parameter U, and use photoemission data to determine the U that best describes the electronic structure of Ce for this system. A direct comparison between photoemission spectra and DFT-based electronic structure has not been made for a phosphate material, and as $CePO_4$ is just one of many phosphates, such as $FePO_4$[46], being investigated as ionic conductors for technological applications, we expect our approach and these results will be of broad interest for both f-electron and phosphate-based solid-state electrolyte materials.

Cerium cations in solid-state compounds can exist in both the 3^+ and 4^+ oxidation states. The nominal charge on cerium in $CePO_4$ is Ce^{3+}, leaving one $4f$ electron on each cerium atom. The highly localized nature of these $4f$ states demands special consideration for the electronic structure of $CePO_4$. For cerium oxides, many groups[22, 47, 48, 49] have recently documented the failure of standard DFT within the local-density or generalized gradient approximations (LDAs and GGAs) due to signicant self-interaction errors associated with $4f$ electron states. For example, erroneous structural parameters have been reported, as well as, in some cases, metallic behavior for Ce-based compounds known to be insulators[50]. A common framework used to address these deficiencies is the DFT +

U method[18]. In this approach, the strong Coulomb repulsion between localized 4*f* states in Ce is treated by adding an effective Hubbard term to the Kohn-Sham Hamiltonian, leading to an improved description of correlation effects in transition-metal oxides. DFT + U requires two parameters, the Hubbard parameter U and the exchange interaction J. Since there is no unique way of including a Hubbard term within the DFT framework[18], different approaches may be adopted. In what follows, we use the rotationally invariant method of Dudarev et al.[51], a standard approach which is summarized in Ref. [51] and elsewhere.

Appropriate values of U for Ce 4*f* electrons have been debated in the literature and several ab initio and empirical values have been reported. Many prior studies use a value around U = 6 eV based on Slater integral calculations of metallic Ce (Ref. [52]) and cerium compounds[53] or optical band gaps and defect formation energies of cerium compounds[48, 54, 55]. However, signicantly smaller values of U have also been reported for cerium oxides based on ab initio calculations[47], and comparison to lattice constants and energies of formation. Fabris et al.[47], for example, used a linear response approach[56] for CeO_2 and Ce_2O_3 and found U = 3 eV (LDA) and 1.5 eV (GGA). All studies noted that both the electronic structure and lattice parameters were somewhat sensitive to the value of U, although in different ways for CeO_2 and Ce_2O_3, indicating that the best choice for U may depend on the environment of the cerium atom. Thus, it is prudent to determine an appropriate value for U by comparison to experiment for cerium in a phosphate environment, where Ce would be expected to behave differently than in cerium oxides or pure metal, rather than adopting values found in the literature for other cerium compounds.

In the following sections, ground-state structure and electronic properties of $CePO_4$ are computed using DFT + U for several different values of U and compared with x-ray diffraction (XRD), x-ray photoemission spectrometry (XPS), and AC impedance spectroscopy experiments on sintered, polycrystalline samples. We propose an optimal value of U that results in calculated electronic structure in agreement with measured photoemission near the valence-band edge. This approach to determining U has yet to be used in ab initio studies of cerium compounds. We show that our value of U provides structural parameters that agree well with XRD measurements, thus providing a necessary foundation for future calculations of electron and proton conductivity, defect energetics, and redox reactions associated with the electrolytic performance of $CePO_4$.

3.2 Experimental Methods

Cerium orthophosphate powders, purchased from Alfa Aesar, are heat treated for 1 h at 800 °C in order to convert from the hydrated rhabdophane to the monoclinic phase. Powders are ground and sieved through 325 mesh, and then ball milled in isopropyl alcohol with 2 wt% polyvinal butyral, dibutyl phthalate, Menhaden Fish Oil (from Aldrich, Mallinckrodt, and Sigma, respectively) for 24 h. The powders are dried, ground, and sieved again, and then uniaxially die pressed at 2000 psi into pellets. Pellets are heated at 600 °C for 1 h to remove binders and then heated at 1200 °C for 5 h for sintering. XRD scans of powders and pellets are performed on a Philips PW3040 XPert Pro diffractometer using the Cu $\kappa\alpha(\lambda = 1.5406$ Å) source operated with a 45-keV x-ray tube voltage.

A Kratos AXIS-NOVA hemispherical electron analyzer is used for the measurement of XPS. The monochromatic Al Kα (photon energy = 1486.6 eV) is used as the x-ray source, and the total energy resolution is set to about 0.4 eV. The pass energy and dwell time of photoemission spectra is set to 20 eV and 100 ms, respectively. Prior to the XPS measurement, the sample surface is lightly sputtered with argon to remove any surface contamination. Sputtering does not change the oxidation state, as was shown by Glorieux in the $CePO_4$ spectra of the 3d binding energies[57]. A small charging effect is present during the measurement and a low-energy electron flood gun is utilized when necessary. All elements in the sample are identied from a survey scan and the chemical state of each element is also confirmed. In order to compare the DFT density of states (DOS) to the photoemission spectra, the Shirley background is subtracted from measured valence-band spectra to remove the effects of inelastic scattering[58].

3.3 Computational Methods

To compute the structure and electronic properties of $CePO_4$, we use DFT + U with both the local spin-density approximation (LSDA or, for short in this work, LDA) and the spin-dependent GGA[17]. All results are obtained using the projector augmented-wave (PAW) method[43] as implemented in the Vienna ab initio Simulation Package (VASP)[41, 42, 59]. For comparison with XPS, spin-orbit coupling and the Perdue-Burke-Ernzerhof (PBE0) hybrid functional is also employed[60]. We treat explicitly 12 electrons for cerium ($5s^2 5p^6 6s^2 5d^1 4f^1$), five for phosphorus ($2s^2 2p^5$), and six for oxygen ($2s^2 2p^6$). Brillouin zone integrations are performed with a Gaussian broadening of 0.1 eV during all calculations, a 6 x 6 x 6 Monkhorst-Pack k-point mesh with the original packing scheme[44], and a 600-eV plane-wave cutoff, all of which result in good convergence of the ground-state properties reported here. Energies are converged to 10^{-6} eV and Hellmann-Feynman forces on the ions are converged to 10 meV/Å. The equilibrium cell volume and shape are determined by optimizing all internal degrees of freedom with different functionals and values of U. The bulk modulus is calculated two ways, first by relaxing the ion positions only and second by relaxing the cell shape and ion positions. Both values are found to be consistent, and the latter is reported. The range of volumes used for the bulk modulus calculations is within 4%-5% of the minimum volume.

As described above, it is well known that standard approximations to DFT, with or without gradient corrections, may incorrectly capture the electronic structure of materials with localized *d* or *f* states. In this work, we use a standard DFT + U framework, described in detail by Dudarev *et al.*[51], to correct for self-interaction errors associated with the Ce 4*f* states. In this approach, only an effective Hubbard parameter U_{eff} = U - J enters the Hamiltonian. Here, we vary U_{eff} (which we simply refer to as U from here on) from 0 to 5 eV. (The standard DFT result corresponds to U = 0 eV.)

3.4 Results and Discussion

3.4.1 Structural properties

The monoclinic phase of $CePO_4$ assumes a structure with $P2_1/n$ symmetry (Figure 3.1)[61]. All atoms sit on sites that have the same symmetry and assume the 4e Wyckoff position, with coordinates A (x, y, z), B (-x, -y, -z), C (-x+1/2, y+1/2, -z+1/2), and D (x+1/2, -y+1/2, z+1/2). There is a single unique cerium site, one phosphorous site, and four oxygen sites. $CePO_4$ is known to be antiferromagnetic (AFM) below a Néel temperature of 77 K[62]. Since there are four cerium atoms in the unit cell, for AFM ordering two must be spin up and two must be spin down (Figure 3.1). For U = 0, our calculations of different spin congurations indicate the ground state is ferromagnetic; for U $\geq$ 1 eV, however, our calculations predict the lowest-energy spin arrangement is indeed AFM, in agreement with experiment, as shown in Table 3.1. A small but non-negligible amount of hybridization between cerium 4*f* and oxygen 2*p* states suggests that the AFM ordering found for finite values of U is mediated by superexchange. In the AFM ground state, each cerium atom has six Ce nearest neighbors; two neighbors are spin aligned and four are antialigned. For the remainder of the work, we assume the spin arrangement shown in Figure 1 for all calculations. Using a simple Heisenberg model, it is difficult to explain the high energy of AF type I compared to other magnetic orderings for all calculations except PBE U = 0 eV. This is especially true because the difference the ferromagnet and AF type III is very small for LDA+U = 3 eV and for this reason the data in Table 3.1 has not yet been published.

As expected, we find that the DFT + U approach within LDA generally results in smaller lattice parameters than the experiment for all values of U explored, leading to a 7% reduction in volume relative to room-temperature measurements. In contrast, GGA-PBE predicts lattice parameters larger than experiments for all values of U, leading to an overestimation of the volume by at most 4%, as shown in Table 3.2. In general, a larger U results in a larger predicted volume, although the change in volume for reasonable U is far less than typical errors associated with the LDA and GGA. In all cases, computed Wyckoff positions are in very good agreement with experiment and independent of U, as can be seen Table 3.3.

For LDA, the monoclinic angle β (Figure 3.1) is computed to be between 103.3° and 103.6° depending on U, which brackets the experimental value of 103.47°. For GGA-PBE, the range of computed β values is between 103.8° and 104.0°. The experimental bulk modulus has not been reported, but the calculated values for GGA-PBE range between 99 and 103 GPa and the LDA values range between 123 and 133 GPa (Table 3.2).

In summary, there is minimal variation in the structural parameters with U, aside from a slight increase in volume and bulk modulus with increasing U. Since a detailed comparison of calculated structural parameters to experiment does not point to a single "best" value of U, in what follows we suggest an optimal U for Ce in $CePO_4$ through comparison to measured photoemission spectra.

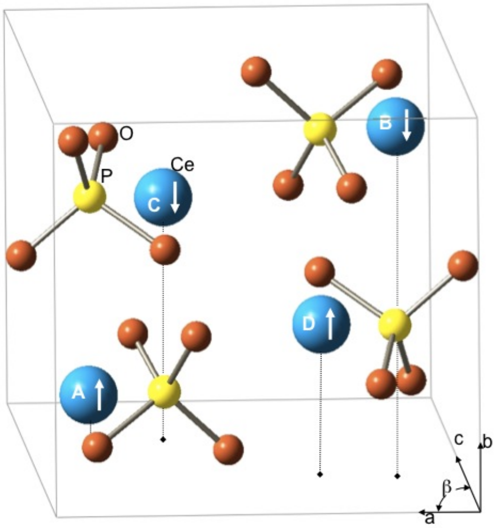

Figure 3.1: The conventional $CePO_4$ unit cell. The lattice vectors are a, b, and c, while the angle between a and c is β. The cerium cations are shown in blue, and the tetrahedra are made of orange oxygen atoms and yellow phosphorus atoms. An antiferromagnetic spin ordering of the cerium atoms is indicated with up and down arrows.

3.4.2 Electronic and magnetic properties

In Figure 3.2, we plot the DOS for $CePO_4$ for all the different values of U (in the PRB publication we only showed a few). In contrast to the lattice parameters, the computed

Table 3.1: The three possible antiferromagnetic structures and the ferromagnetic structures show type III has the lowest energy. Using the labels in Figure 3.1, AF type I has Ce(A) and Ce(B) coupled ferromagnetically. AF type II has Ce(A) and Ce(C) coupled and AF type III has Ce(A) and Ce(D) coupled, which is used for all calculations and shown in Figure 3.1.

ΔE (eV)	PBE U = 0 eV	U = 3 eV	LDA U = 0 eV	U = 3 eV
ferromagnet	minimum	0.4543	minimum	0.00004
AF type I	0.0144	0.82068	0.1519	0.7464
AF type II	0.1486	0.00001	0.0808	0.00022
AF type III	0.1521	minimum	0.0847	minimum

Table 3.2: The volume and lattice parameters for the measured and calculated $CePO_4$ unit cell are shown for all U (in eV). The experimental bulk modulus (B) has not been reported.

Functional		Volume (Å^3)	a (Å)	b (Å)	c (Å)	β°	B (GPa)
Experiment		300.60	6.8004	7.0231	6.4717	103.460	NA
LDA	U=0	287.37	6.6935	6.9266	6.3705	103.357	125
	U=1	287.98	6.6999	6.9302	6.3740	103.331	132
	U=2	298.46	6.7083	6.9465	6.3897	103.561	122
	U=3	290.20	6.7141	6.9515	6.3934	103.464	129
	U=4	290.99	6.7181	6.9597	6.3993	103.455	133
	U=5	291.51	6.7204	6.9616	6.4040	130.351	133
PBE	U=0	308.42	6.8956	7.0893	6.4980	103.849	99
	U=1	309.20	6.8944	7.0981	6.5079	103.862	100
	U=2	309.80	6.9263	7.0741	6.5166	104.010	99
	U=3	310.84	6.9091	7.1084	6.5195	103.883	103
	U=4	311.64	6.9138	7.1174	6.5245	103.908	102
	U=5	312.38	6.9156	7.1235	6.5304	103.832	103

Table 3.3: Atom positions (in reduced units of the lattice parameters) for U = 0 and 3 eV.

		Experiment	LDA U = 0 eV	LDA U = 3 eV	PBE U = 0 eV	PBE U = 3eV
Ce	X	0.2818	0.2800	0.2813	0.2852	0.2860
	Y	0.1591	0.1587	0.1586	0.1583	0.1586
	Z	0.1000	0.1032	0.1023	0.0992	0.0991
P	X	0.3050	0.3039	0.3047	0.3039	0.3046
	Y	0.1663	0.1642	0.1641	0.1621	0.1621
	Z	0.6124	0.6144	0.6136	0.6116	0.6111
01	X	0.2494	0.2486	0.2494	0.2498	0.2505
	Y	0.0059	0.0041	0.0047	0.0057	0.0061
	Z	0.4439	0.4438	0.4433	0.4405	0.4405
02	X	0.3813	0.3817	0.3827	0.3813	0.3822
	Y	0.3314	0.3343	0.3333	0.3311	0.3303
	Z	0.4995	0.4964	0.4959	0.4987	0.4984
03	X	0.1061	0.4771	0.4770	0.4714	0.4714
	Y	0.2163	0.1067	0.1084	0.1034	0.1035
	Z	0.8040	0.8096	0.8089	0.8067	0.8061
04	X	0.1282	0.1243	0.1256	0.1273	0.1282
	Y	0.2163	0.2158	0.2158	0.2124	0.2125
	Z	0.7086	0.7152	0.7136	0.7099	0.7086

electronic structure depends signicantly on the value of U, as expected. Notably, despite the fact that $CePO_4$ is known to be an antiferromagnetic insulator, $CePO_4$ is computed as metallic and ferromagnetic for U = 0, with the Fermi level positioned within the $4f$ states. However, for U $\geq$ 1 eV, the partial self-interaction correction associated with U reduces the occupied levels relative to the unoccupied states in the $4f$ manifold, opening an energy gap, and $CePO_4$ is correctly predicted to be insulating and antiferromagnetic. The band gap is found to grow with increasing U, as shown in Figure 3.2. There is sharp peak at the valence-band edge associated with a lone Ce $4f$ electron per atom, reflecting a 3^+ oxidation state for the Ce cation (conrmed via examination of the partial DOS).

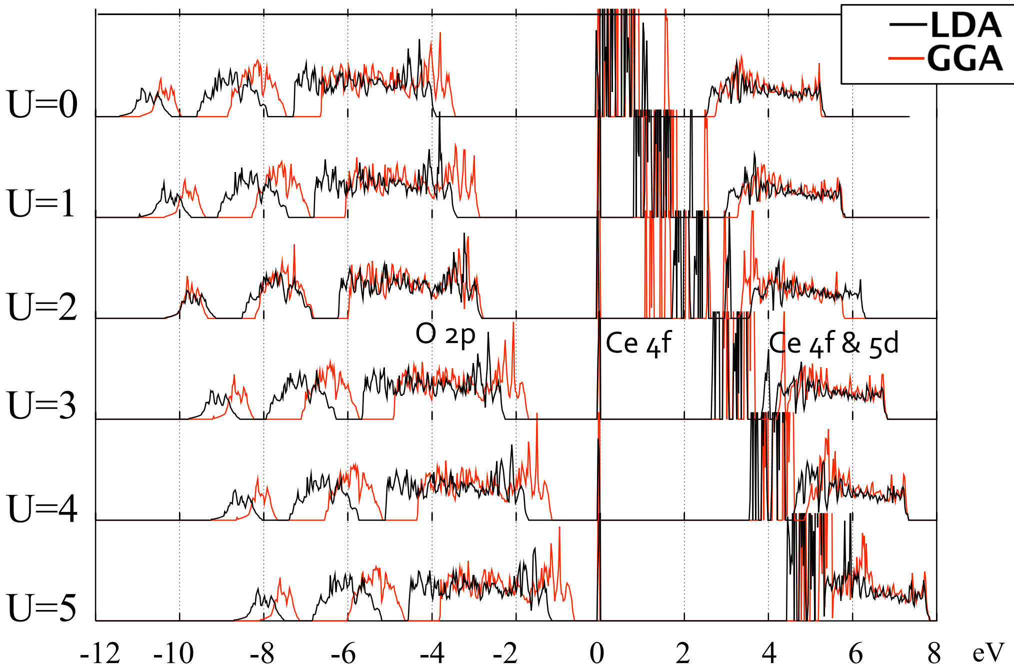

Figure 3.2: The valence and conduction bands for U = 0-5 show the gap opening, where the black is the LDA functional and the red is the GGA functional. The Fermi energy is set to 0 eV and the orbital assignments at the top of the plot are from the partial DOS (which is not shown).

Figure 3.2 also shows that the gap between this occupied Ce $4f$ band and the top of the oxygen $2p$ band - which will be referred to as the valence gap - *decreases* with increasing U (peaks labeled in Figs. 3.2 and 3.3). Although U reduces the spurious self-interaction for $4f$ electrons, lowering the average energy of the occupied $4f$ bands, it does not affect the energetics of the O $2p$ band. In what follows, the valence gap is calculated as a function of U as the difference between energy levels at the M point, which represents the location of the direct valence gap between bands, as shown in Figure 3.3, where the full band structure is plotted.

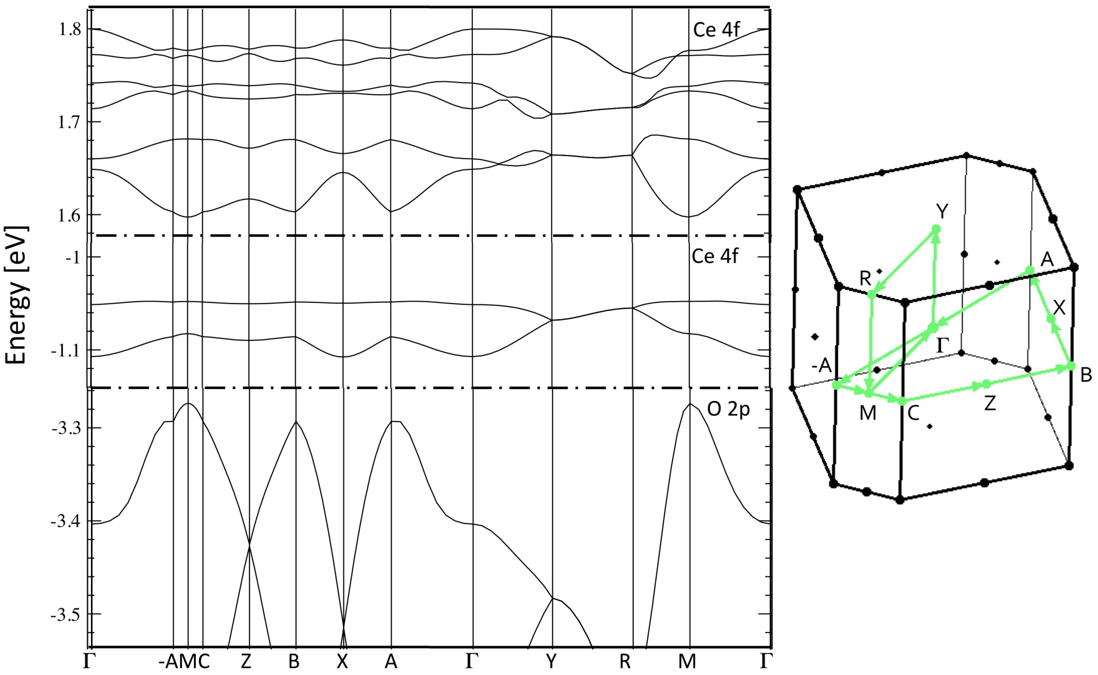

Figure 3.3: The band structure for LDA U = 3 eV was calculated along lines between high symmetry points in the first Brillouin zone, which are given in the plot to the left-hand side. High symmetry points provided in reduced coordinates of the primative reciprocal lattice vectors are Γ (0,0,0), A(-0.60,0,0.41), B (0.40,0,0.41), C (-0.40,0,0.59), M (-0.5,0,0.5), R (0.5,0.5,0.5), X (0.5,0,0.5), Y (0,0.5,0), and Z (0,0,0.5).

Figure 3.3 lends insight into the difference in conductivity between the lanthanum and cerium orthophosphates. p-type doping would lead to a partially occupied $4f$ band at the Fermi-level valence band, and extraordinarily heavy holes (about 1000m$_e$, where m$_e$ is the electron mass) within an effective mass picture, due to the flatness of the bands. Interestingly, this would support hypotheses put forth in the literature that in oxidizing conditions conductivity is due to electron-hole hopping rather than proton transport based on the lack of H/D isotope effect[8] and the activated behavior of electronic conductivity seen in $CePO_4$.

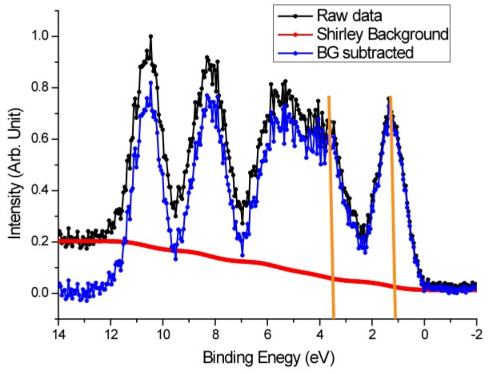

Figure 3.4: The energy difference between the first two valence bands, measured peak to peak, is 2.5±0.2 eV.

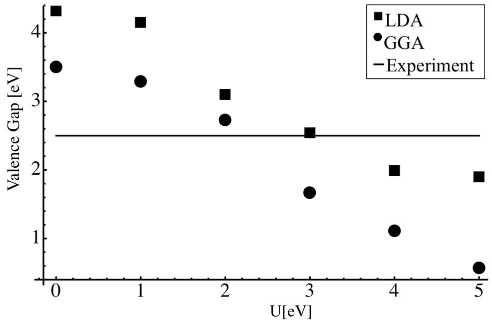

Figure 3.5: The energy difference between these two bands as measured by DFT + U for U = 0-5 eV is plotted for LDA and GGA.

In Figure 3.4, we show the measured photoemission data taken on high-purity cerium orthophosphate powders. From Figure 3.4, the measured valence energy gap is 2.5 ± 0.2 eV. As photoemission measures ejected electrons, it provides a good measure of the occupied DOS. The quasiparticle spectrum measured by photoemission can differ significantly from the Kohn-Sham DOS. Self-energy corrections to the Kohn- Sham energies, within the GW approximation, for example, can account for these differences and lead to quantitative agreement with experiments[63, 64]. In what follows, we adjust U, which can be viewed as a model self-energy correction to the $4f$ states, until the valence gap agrees with the photoemission measurement.

In Figure 3.5 we plot the computed valence gap as a function of U for both LDA and GGA. As U partially corrects for the self-interaction associated with the $4f$ states, it will reduce their average energy relative to the O $2p$ band, causing a decrease in the valence gap with increasing U. The values of U that result in a valence gap closest to experiment are U = 3 eV for LDA and U = 2.5 eV for GGA. (We note that in determining these values, we have used the fully optimized geometry for each of the two exchange-correlation functionals at a given value of U.) Interestingly, the computed valence gap does not decrease linearly with increasing U; it contains an inflection point for both LDA and GGA, as shown in Figure 3.5. This "crossover" separates values of U large enough so that unoccupied Ce $4f$ states begin to overlap with the Ce $5d$ bands. Figure 3.5 indicates a leveling off of the valence gap after U = 4 eV for LDA, which implies that this value of U is large enough to account for a majority of the self-interaction of the $4f$ orbitals, and that larger values will not significantly change the electronic structure. This "leveling off" is not observed for GGA up to 5 eV, though this may not be surprising since the inflection point in Figure 3.5 occurs for a larger value of U for GGA than for LDA.

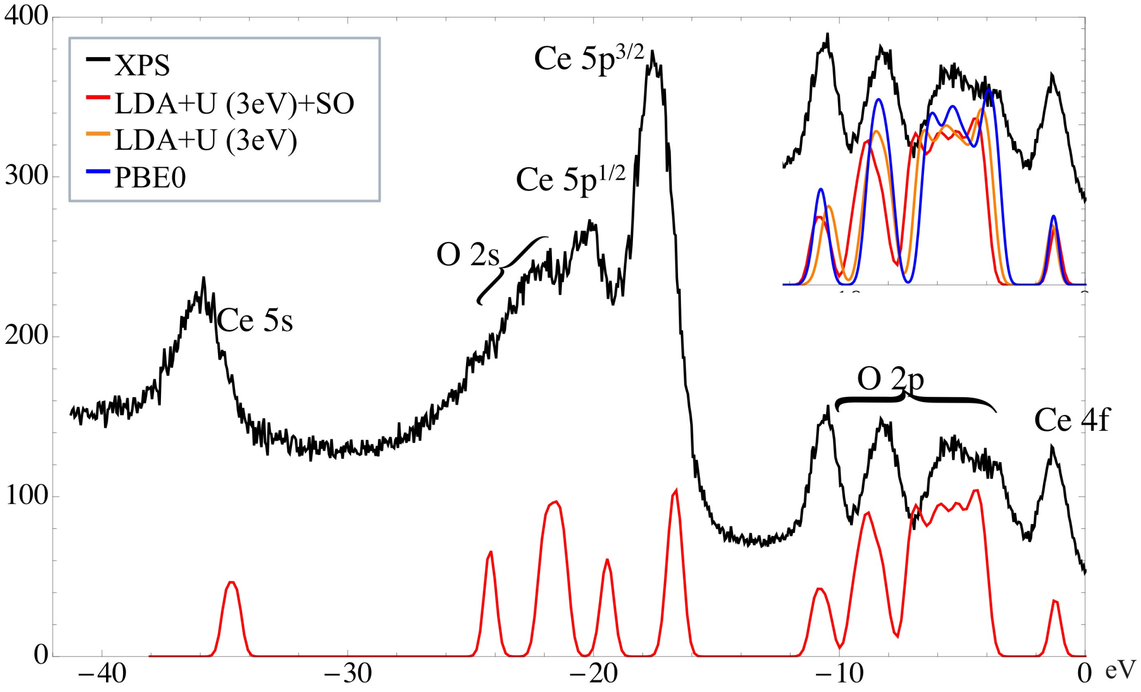

Figure 3.6: The valence-band photoemission spectra is plotted along with the calculated DOS with Gaussian smearing for the LDA + U (3 eV) plus spin-orbit (SO) coupling. The inset in the upper right-hand side compares the LDA + U and PBE0 near-valence-band edge spectra. The peaks are assigned via the calculated partial DOS, and are supported by known XPS binding energies.

In Figure 3.6, we present a direct comparison of the measured photoemission spectrum of $CePO_4$ and our first-principles calculations over a broad energy range. As described above, near the valence-band edge the spectrum is best fit with U = 3 eV for LDA. Peaks in the photoemission are assigned using a site- and orbital-projected DOS (not shown). Our assignments are very consistent with known literature values of the binding energies of these semicore states (calibrated using the Ce $3d$ peaks)[65]. To better capture the energetics of Ce states further below the valence-band edge, spin-orbit corrections are also obtained with the VASP code, assuming noncollinear spins on the Ce ions[66, 67]. For U

= 3 and within the LDA, we compute a 3-eV splitting of the Ce 5p orbitals, similar in magnitude to that predicted for CeF_3[68]. (As expected, spin-orbit coupling has negligible influence on the electronic structure near the valence-band edge.) We also compare our U = 3 eV LDA calculations with those using a hybrid functional, PBE0 (Refs. [60] and [69]), which contains 25% Fock exchange. Use of hybrid functionals is an alternative to DFT + U, as they partially mitigate self-interaction errors for all states, not just the Ce 4f levels. We find small differences between the computed DOS for LDA U = 3 eV and PBE0 for states further from the valence-band edge, as expected; but from the inset of Figure 5, the PBE0 valence gap is in good agreement with LDA U = 3 eV, indicating that even when self-interaction corrections are also applied to O 2p states, fitting the Ce 4f U to the valence gap with a simpler DFT + U approach results in an acceptable electronic structure for this compound.

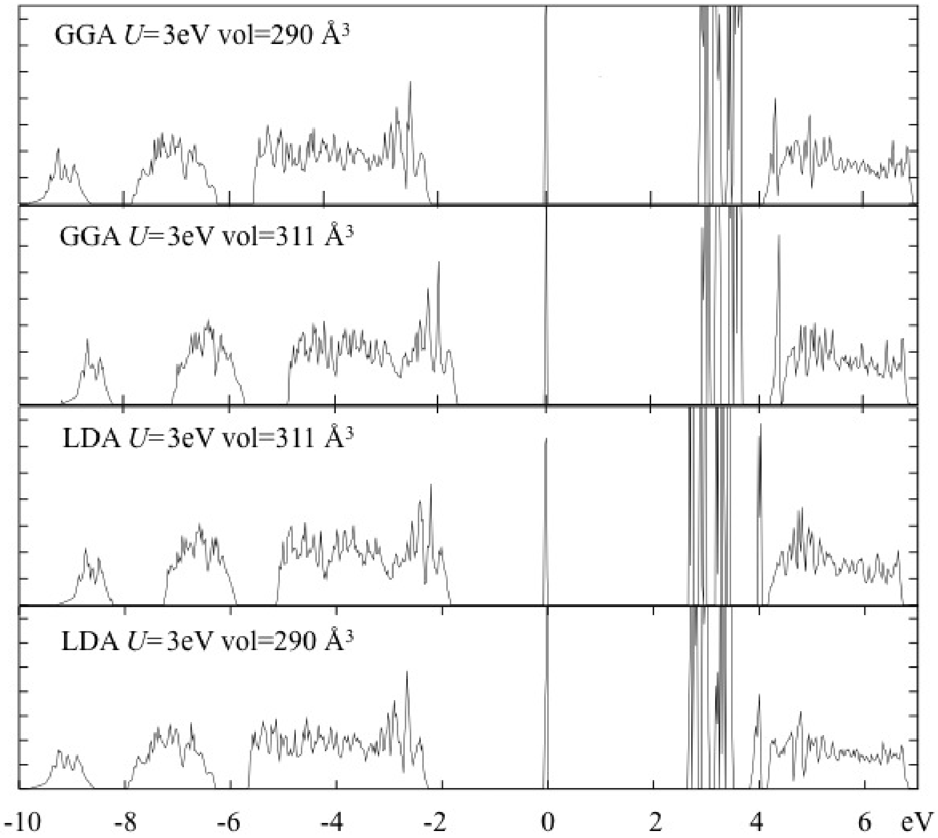

Figure 3.7: The density of states near the top of the valence band (set to zero in each case) is plotted for PBE and LDA+U=3eV for a unit cell with volume = 290 and 311 Å^3.

Finally, we examine the question of why the LDA and GGA-PBE lead to different values of U, about 0.5 eV less for the GGA + U than LDA + U through comparison with photoemission experiments. We find that this distinction is primarily a consequence of the difference in the equilibrium volumes for the two functionals. We compute the DOS with LDA + U = 3 eV with the volume artificially fixed at the GGA + U = 3 eV volume (310.84 Å^3) and compare the result directly with LDA + U = 3 eV DOS at its true optimized volume (290.20 Å^3). A similar "computational experiment" is performed using GGA + U = 3 eV at both LDA + U and GGA + U volumes (290.20 and 310.84 Å^3, respectively). These DOS are shown in Figure 3.7.

For fixed volume and U, LDA + U and GGA + U yield very similar valence gaps (between Ce $4f$ and O $2p$). Interestingly, however, the band gap (between occupied and unoccupied $4f$ states) does depend somewhat more on the type of exchange-correlation functional. In sum, these "computational experiments" show that while specifics of the functional play a small role in the electronic structure, the valence gap (and value of U that best fits it) is most sensitive to cell volume. We note here that since the LDA and GGA used here bracket the experimental volume, our work demonstrates that for $CePO_4$, U lies in the range of 2.5-3 eV.

3.4.3 Modeling the Hole with Sr-doping

In order to model 3% Sr-doping and polaron conductivity in $CePO_4$, a large 2x2x2 supercell must be employed. Electronic convergence is very difficult to achieve and results are difficult to reproduce, so the following data are somewhat preliminary and further work would be warranted prior to publication. Nevertheless, the trends observed in the calculations are in reasonable good agreement with initial XPS studies, and are included in this dissertation for completeness. Either a proton or a hole can charge-compensate for the aliovalent Sr-dopant and 2x2x2 supercells with Sr and proton dopants will converge. On the other hand, a few cells with just a Sr-dopant will localize the hole into a polaron, while the majority of others will not converge and show metallic-like charge sloshing, no matter what value of U is chosen.

For the cells that did converge, the hole is localized on a Ce atom near the Sr dopant, as seen in the inset of Figure 3.8. It seems to prefer a Ce with the same magnetic Wyckoff position (A, B, C, or D) rather than the closest Ce to the dopant. In order to model conductivity, the activation energy for polaron hopping from one Ce to a neighbor is necessary, but so far has remained elusive since converging the polaron on different Ce atoms has proven difficult. Still, the DFT DOS with 6% Sr-doping in a 2x2x1 supercell can capture features seen in the XPS, such as the stronger binding of most of the electrons (shifting down of the DOS) and extra peaks due to the $5p$ electrons of the Sr dopant.

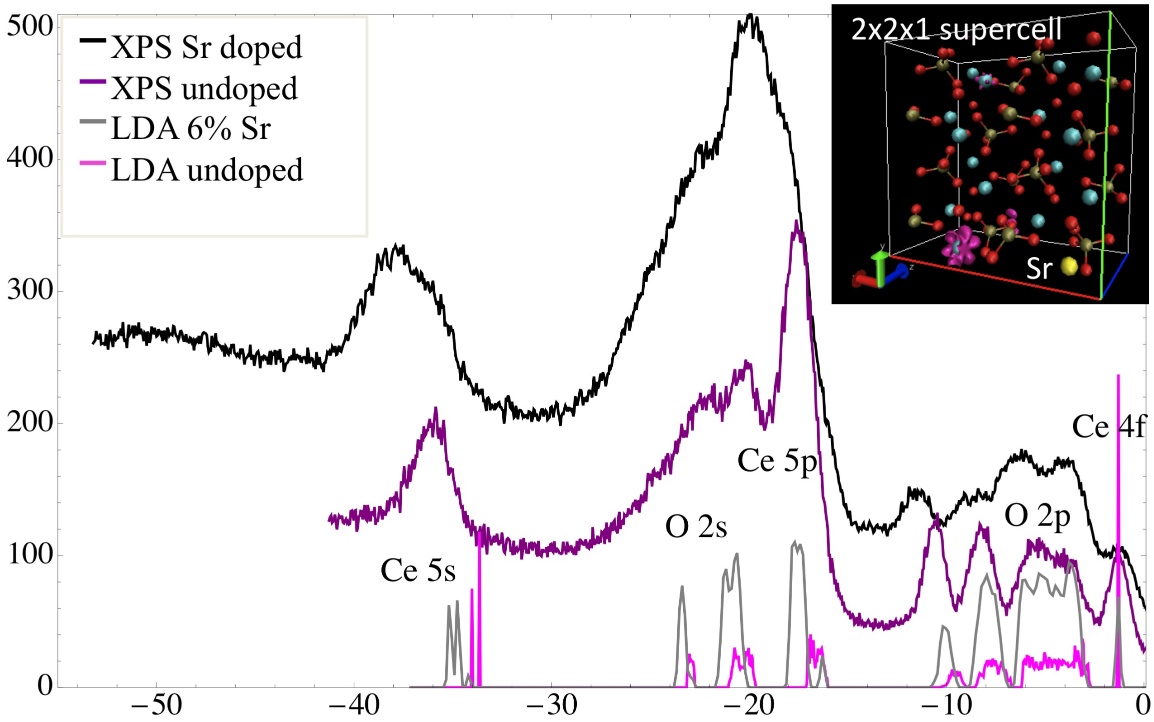

Figure 3.8: The DOS from XPS and DFT for Sr doped $CePO_4$ is compares well to the undoped DOS. The shoulder near the Ce 5p peak in the Sr-doped XPS (black spectrum) can be seen in the gray DFT DOS. Addition of Sr causes all peaks to shift towards lower energies, which is also captured in the DFT calculation; the gray Sr-doped DOS looks stretched compared to the pink undoped DOS. In the upper right hand corner, the isosurface of the energy associated with the hole in a 2x2x1 supercell shows that the hole is localized on a Ce near the Sr-dopant.

3.5 Conclusions

The ground-state geometry and electronic structure of $CePO_4$ was investigated with x-ray diffraction and photoemission, and a DFT + U method for Hubbard-like effective U values ranging from 0 to 5 eV. We found that structural properties, including lattice parameters and bulk moduli, are not sensitive to U. In contrast, the electronic structure is strongly sensitive to U near the band edges, as expected. By direct comparison with experiments, we found that the U values for Ce $4f$ states in $CePO_4$ that provide the best match for experiments were between 2.5 and 3 eV. More specically, we computed that U = 3 eV for the LDA functional and U = 2.5 eV for the GGA-PBE functional by comparing directly to the “valence gap”, defined here as the difference between the bottom of the occupied $4f$ and the top of the occupied O $2p$ valence bands. The smaller value of U for GGA can be primarily associated with its larger unit-cell volume. Using a DOS computed with LDA + U = 3 eV, all peaks in the photoemission spectrum could be assigned with confidence. The use of the nonempircal PBE0 functional to calculate the DOS confirmed that even when self-interaction errors are treated for all states, fitting the valence gap is acceptable to fix the U for Ce $4f$ electrons. The calculations presented here show the importance of using photoemission spectroscopy for validating U parameters. This work sets the stage for further theoretical work on proton hopping in $CePO_4$ and the electronic structure of aliovalently doped and oxygen-decient $CePO_4$, and will inevitably lend insight into the nature of the mixed conduction of this proton-conducting material.

Chapter 4

First–prinicples calculation of small polaron mobility in hematite

The mobility of electron small polarons in hematite, α–Fe_2O_3, is calculated with planewave density functional theory methods and Hubbard–U corrections (DFT+U) in periodic supercells. The results compare well to previously published wavefunction–based calculations on small clusters [70, 71]. By setting the effective Hubbard–U parameter to 4.3 eV, the activation energy for nearest–neighbor transport is calculated to be 0.13 eV and the room–temperature mobility is estimated as 0.02 S*cm^2/s, which are very close to the experimental values of 0.118(2) eV and 0.04 S*cm^2/s [72].

4.1 Introduction

Charge transport in many insulating materials occurs by the conduction of localized electrons or holes, known as small polarons. For applications including batteries[73], thermoelectrics [74], photovoltaics[75, 76], and catalysts for water–splitting [77, 78], solid–oxide fuel cells [79], and oxidation of organic compounds [80], the magnitude of the small polaron mobility has a significant effect on the technology's performance. The broad practical interest in polaron mobilities has motivated a number of recent efforts aimed at the development of methods for computing transport properties from electron–structure calculations[73, 81]. In the present work we explore the accuracy of approaches based on density functional theory (DFT), focusing on computing small polaron mobilities in hematite, α–Fe_2O_3, a system for which previous calculations based on wavefunction–based methods[70, 71] and experimental results [72] are available. Hematite is the subject of current research due to its favorable properties for water splitting [82, 83].

Conduction of small polarons is an activated process, which can be experimentally observed by the increase in conductivity with increasing temperature, in sharp contrast to band–like conductivity in metals or some semiconductors. Small polarons are localized electrons or holes that polarize the lattice around them, thus self–trapping in a potential energy well. Small polarons are differentiated from large polarons in that they are more localized, so their spatial extent is small and the area of the lattice distortion is confined to about a lattice parameter. Small polaron hopping from an initial potential energy well to another minima requires thermal oscillations to transfer the lattice polarization from site to site and involves overcoming an activation energy barrier, which can be determined experimentally and computationally.

The theory of electron transfer in solution was first presented by Marcus in 1956[84] and has been successfully applied to small polaron hopping in solid–state materials. In limiting cases where the transfer falls into the so–called "adiabatic" or "diabatic" regimes, the transfer rate, τ can be expressed in the following form:

$$\tau = A \exp\left(\frac{-\Delta G^{\ddagger}}{kT}\right). \tag{4.1}$$

A is a pre–exponential factor and $\Delta G^{\ddagger}$ denotes the activation energy barrier. The extent of the coupling of the electrons to the thermal oscillations of the lattice determines whether the transfer is in the adiabatic or diabatic regime. Specifically, following Ref [85], the nature of the hopping mechanism can be ascertained based on the value of the adiabadicity criterion, γ, defined as

$$\gamma = \frac{1}{h\nu_{\text{eff}}}\left(\frac{\pi}{4\Delta G_{\text{ad}} kT}\right)^{\frac{1}{2}} \mathrm{V}_{AB}^{2}. \tag{4.2}$$

In Eqtn. 4.2, V_{AB} gives a measure of the strength of coupling between the electron and the lattice at the transition state and is called the electronic coupling matrix element, kT is the thermal energy, h is Planck's constant, ν_{eff} is the effective frequency for motion along the reaction coordinate, and ΔG_{ad} is the adiabatic activation energy barrier.

The probability of charge transfer is 1–exp[-γ] and if γ is much less than 1, the transfer is in the diabatic regime (non–adiabatic) and follows Fermi's golden rule for charge transfer rates. In this case, small coupling between the electron and lattice indicates that the Born–Oppenheimer approximation does not hold because the electrons cannot quickly follow the nuclei motion and instead remain localized on the initial ion during the timescale of phonon periods (hence the term non–adiabatic). On the other hand, if the electronic coupling is large compared to the activation energy barrier, the transfer is adiabatic. In this case, the adiabatic activation energy barrier, ΔG_{ad}, decreases by V_{AB} from the diabatic activation energy barrier, ΔG_{dia}, such that $\Delta G_{\text{ad}} = \Delta G_{\text{dia}} - \text{V}_{AB}$. Thus, knowledge of V_{AB} allows one to determine the nature of the transfer process, since γ is small if V_{AB} is small compared to ΔG_{ad}.

Calculation of the polaron transfer rate as described in the Marcus formalism has been widely applied using wavefunction based methods for complex metal oxides[70, 71, 81, 86, 87, 88, 89, 90]. In many of these studies, the electronic coupling, V_{AB}, is calculated using a cluster that is excised from a relaxed periodic supercell (which was previously employed to calculate ΔG_{dia}). An alternative approach, explored in the current work, is to use DFT methods with planewave bases. DFT approaches offer the advantage of being able to efficiently treat very large supercells, which can be used to model dilute or extended defects such as surfaces[91]. The main drawback of these methods is the need to add corrections beyond DFT to account for the self–interaction and correlation errors, which can hinder the localization of polarons.

Unfortunately, the current literature on polaron transport does not offer a standardized or well–tested method for computing polaron mobilities within DFT. There have been relatively few calculations with constrained DFT[92, 93] or DFT plus the Hubbard–U (DFT+U)[73, 94, 95, 96, 97]. In the present work, we employ an approach similar to that proposed by Maxisch, Zhou, and Ceder[73] for computing adiabatic activation energies for small polarons with DFT+U. We extend their approach by presenting a method for estimating V_{AB} at the relaxed transition state, i.e. the saddle point, and also by calculating the prefactor for hopping rates.

As alluded to above, DFT within the local or semi–local approximations for the exchange–correlation potential often fails to correctly describe highly localized electrons such as polarons and ‘d’ electrons in transition metals or ‘f’ electrons in actinides due to the self–interaction error and missing correlation. The addition of a Hubbard–U correction [51] is an inexpensive and practical way to overcome these limitations and is determined either empirically or self–consistently with linear response theory[56]. When a small polaron sits on a metal ion, the Hubbard–U can help to localize the polaron in a ‘d’ or ‘f’ like orbital and keep it from forming delocalized states. Thus, the electronic structure of doped hematite and other iron oxide compounds has been accurately calculated with DFT+U[98, 99]. If the polaron instead sits on an oxygen ion, like in TiO_2, other methods of localizing the charge are necessary[93].

In the present work we explore the use of DFT+U methods in the calculation of electron small polarons in α–Fe_2O_3. Henceforth, ‘polaron’ will be used to specify ‘electron small polaron’, unless otherwise specified. We focus on electron–polarons in this material because it is a native n–type material, for which polaron mobilities have been measured experimentally and computed previously by wavefunction–based methods [70, 71, 72]. These previous studies allow us to determine the relative accuracy of the DFT+U approach compared to measurements and calculations performed with a completely independent methodology. To the best of our knowledge no direct comparisons of DFT+U and wavefunction–based methods have been performed to date for the same material.

4.2 Computational Methods

α–Fe_2O_3 has the corundum–type structure with a $R\bar{3}c$ space group (neglecting spin), in which the oxygen ions are hexagonal close packed and form stacked octahedra, as in Figure 4.1. In the calculations with polarons, we employ 2x2x1 supercells of the hexagonal unit cell. The hexagonal unit cell contains four formula units, while the primitive cell is rhombohedral with two formula units, which we use to calculate the phonon spectrum provided in the Appendix. The N*é*el temperature is 953 K[100], so hematite is antiferromagnetic at room temperature and the Fe spins are coupled ferromagnetically in the basal planes above the Morin temperature of 250 K. Polaron hopping is much faster between iron atoms with the same spin, so conductivity in the basal plane is faster than along the c–axis at room temperature [101].

In order to compare to room temperature mobility measurements, we use the antiferromagnetic structure above the Morin temperature, though this is not the zero–temperature magnetic ground state, which has ferromagnetic coupling along the long c–axis.

For calculation of the mobility, the polaron transfer rate, τ from Eqtn. 4.1, must be known. In particular we focus on transfer of an electron small polaron (Fe^{2+}) to nearest Fe^{3+} neighbors. Figures 4.1 (A) and (B) show the 120 atom supercell at the ground and saddle point, respectively; the two Fe ions highlighted in Figure 4.1 (B) with the extra electrons charge density are nearest neighbors. Determining the attempt frequency and the activation energy barrier involves multiple calculations, so we attempt to clearly present our methods below, starting with the activation energy barrier.

Our approach for calculating adiabatic activation energy barriers starts by determining the ground state of the polaron. The ground–state configuration is determined by adding an extra electron to a cell with a positive background charge and periodic boundary conditions (PBC) and then allowing the ions and volume to relax (as described more fully in the Structure and convergence section).

The resulting ground–state configuration is represented by the state labeled 0 in Figure 4.2. This figure also plots the energy as a function of reaction coordinate for transfer to a neighboring equivalent site (labeled 1) for three different scenarios. The first is given by the dashed grey lines, which represent a sketch of harmonic potential energy wells centered

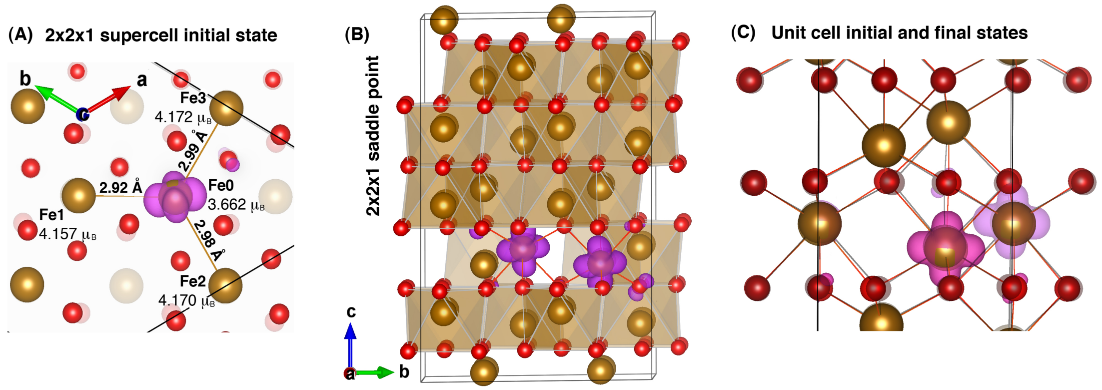

Figure 4.1: (A) The 2x2x1 supercell of α–Fe$_2$O$_3$ at the initial ground state shows three possible polaron trajectories to nearest neighbors Fe1, Fe2, or Fe3 (Fe ions in gold). The polaron, whose extra electron charge density isosurface is shown in purple, has a slight preference to hop to the nearest neighbor Fe1. The bond length between Fe0 and Fe1 is slightly shorter and the Fe1 magnetic moment (shown below the ion label) is smaller than the other two nearest neighbor Fe ions. The black lines give a sense of the **a** and **b** lattice vectors and the red oxygen ions show hexagonal close packing. (B) The 120–atom 2x2x1 supercell at the saddle point shows the polaron is delocalized over the initial and final Fe ions and a few oxygen ions. Extra oxygen ions are included to complete the Fe octahedra. (C) A close–up of the initial (purple) and final (pink) polaron isosurfaces in the hexagonal unit cell shows that the polaron has ‘d’–orbtial character. The lattice polarization around the polaron can be seen, where the initial (purple) configuration is given by the grey bonds and atoms. This image shows that the closest oxygen ions move away from the negatively charged polaron.

on sites 0 and 1, and correspond to the change in energy as a function of the ionic positions along the transition path for the case where the electron remains localized on a specific site. The intersection of the harmonic potentials for the polaron localized on sites 0 and 1 gives the diabatic activation energy barrier (labeled ΔG_{dia} in Figure 4.2), as estimated from our calculation of ΔG_{ad} and V_{AB}.

In the second scenario, the red lines represent a commonly–employed approximation to the adiabatic activation energy (for example Ref. [73]) derived by linearly interpolating the ionic positions between states 0 and 1 and computing the energies for self–consistent charge densities on the Born–Oppenheimer surface corresponding to these different ionic configurations. $\Delta\tilde{G}_{\mathrm{ad}}$ is the difference in energy between the points 0 and 0.5, the transition state (TS), on the Born–Oppenheimer surface. We will call the approximation of the activation energy barrier from the linear interpolation $\Delta\tilde{G}_{\mathrm{ad}}$ and the electronic coupling $\tilde{\mathrm{V}}_{AB}$. In the present work we compute directly $\Delta\tilde{G}_{\mathrm{ad}}$, ΔG_{ad} and V_{AB} for both nearest

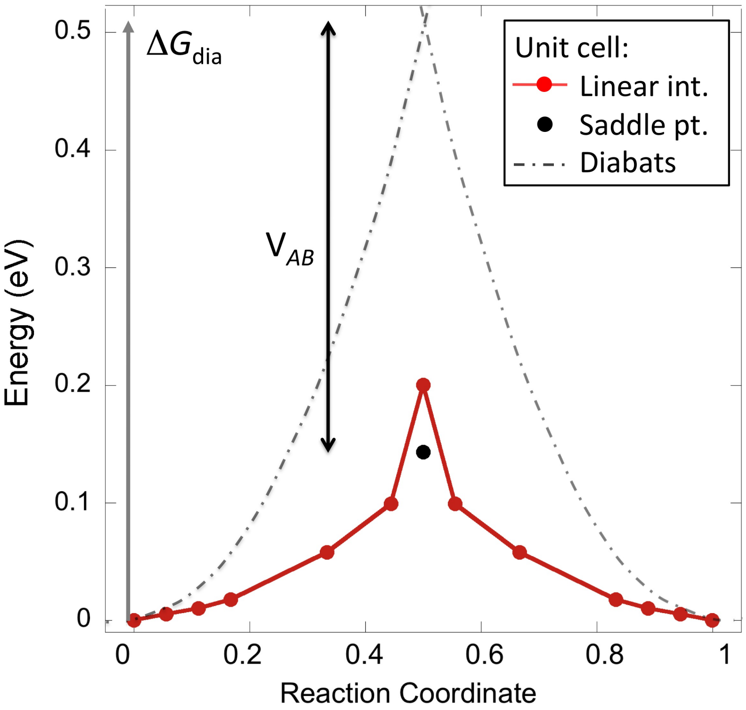

Figure 4.2: The electronic coupling, V_{AB}, lowers the diabatic activation energy barrier, ΔG_{dia}. The diabats and ΔG_{dia} are estimated from our calculation of ΔG_{ad} and V_{AB}. The images from the linear interpolation and the relaxed saddle point are calculated for the 30–atom unit cell with U=4.3 eV.

and next nearest neighbor (nnn) hops of the polaron, as described in more detail below. In this approach, the electronic structure at the transition state and each image along the reaction coordinate is calculated using same supercell size and convergence parameters as the ground state.

Finally, the black solid circle at the transition state represents a refined estimate of the adiabatic activation energy, derived in the present work by performing a force–based relaxation of the ions to the nearest extremum starting from the transition state geometry approximated by linear interpolation. As indicated in Figure 4.2, the transition state geometry at point 0.5, as approximated by a linear interpolation of ionic positions, is found in this work to give rise to a significant overestimation of the true adiabatic activation energy. This is due to the fact that the residual forces on the ions for linearly–interpolated positions are found to be on the order of 0.4 eV/Å and are thus significant. The relaxed geometry is used in phonon calculations to verify that it is a true saddle–point (with one imaginary vibrational frequency and all others real). In the unit cell at the saddle point, we obtain

Table 4.1: Lattice parameters

Lattice parameter	Experiment hexagonal[103]	Calculation: hexagonal	2x2x1 supercell with polaron	Calculation rhombohedral
a	5.04	5.07	10.17	5.4805
b	5.04	5.07	10.17	5.4805
c	13.77	13.88	13.93	5.4805
α (deg)	90	90.0	90.1	55.1
β (deg)	90	90.0	90.0	55.1
γ (deg)	120	120.0	120.0	55.1
z (Fe)	12c 0.355	0.354		4c 0.1470
x (O)	18e 0.306	0.306		6e 0.0560

only one imaginary phonon frequency (14.64i THz) with a corresponding eigenvector that involves displacements of the Fe and O ions along the reaction path.

4.2.1 Structure and convergence

We use DFT with the PBE functional[17] as implemented in the Vienna Ab–Initio Simulation Package (VASP)[42, 59] for our calculations. The PBE–PAW potentials with 8 valence electrons for Fe and 6 valence electrons for O are employed. The electronic wavefunctions are expanded in a planewave basis set with a 650 eV energy cutoff. We use a 2x2x2 k–point mesh for the 120 atom supercell and a 4x4x2 k–point mesh for the 30 atom hexagonal unit cell. Both cells are converged with respect to k–points up to 10^{-4} eV and the supercell uses Monkhorst–Pack[44] while the unit cell is centered at the Gamma point (also some DOS calculations use the Gamma point). For total energy and relaxation calculations, gaussian smearing of 0.03 eV is used, while density of state calculations employ the tetrahedron method of k–point generation. Forces on the ions in the bulk unit cells are converged to 0.001 eV/Å and the forces in the polaron containing cells are converged to 0.01 eV/Å. The criterion for convergence of the self–consistent charge density was a tolerance on the energy change of at most 10^{-7} eV.

We perform collinear spin–polarized calculations with the Fe ions ferromagnetically coupled in the basal planes and antiferromagnetically coupled along the c–axis (see Ref [100] for a figure). The Fe ions are high–spin with a measured magnetic moment of 4.6 Bohr magnetons[102]. The ionic positions obtained from a total relaxation of the bulk hexagonal unit cell is the starting structure for the calculations with the polaron. The lattice parameters and Fe and O Wyckoff positions of the hexagonal unit cell and supercell with the polaron in the ground state (both using U=4.3 eV, as justified in Choice of U section) are given in Table 4.1 and compared to experiment[103].

In order to converge to a state corresponding to a localized polaron on a specific Fe, it is necessary to break the symmetry of the bulk crystal structure, which is done by manually moving one oxygen ion on the order of 0.01 Å, away from its ‘nearest’ Fe atom. When the cell is allowed to relax, the polaron formation is noted by the change in the magnetic moment on the nearest Fe atom and the change in bond lengths (see Figure 4.1 (A) and (C)). The localization of the electron can also be seen by plotting the charge density associated with the extra electron, and by analyzing the electronic density of states (DOS). Figure 4.3 shows the DOS obtained in such a calculation with an effective Hubbard–U parameter value of 4.3 eV; the state corresponding to the extra localized electron corresponds to the sharp peak nearest the Fermi energy.

For the most accurate saddle point calculations, we use 120 atom 2x2x1 supercells, where the c–axis is not doubled. Calculation of ΔG_{ad} in the 30 atom and 120 atom cell allow us to estimate the effect of system size. A larger supercell than the 120 atom supercell is deemed unnecessary since the activation energy from the saddle point obtained from this supercell is at most only 0.02 eV smaller than in the 30 atom unit cell.

4.2.2 Transition states

All Fe atoms are related by symmetry in the bulk crystal, such that the initial and final states of the polaron in the same basal plane are identical. Thus, once the ground–state configuration (ionic positions) of the polaron is determined on the initial Fe, a symmetry operation moves the polaron configuration from the initial to the final Fe.

There are only three nearest neighbor Fe^{3+} ions to the initial Fe^{2+} ion (the polaron containing iron) in the same basal plane and these converge to different bond lengths from the initial Fe ion (2.92, 2.98, and 2.99 Å) in the 120 atom supercell as shown in Figure 4.1 (A) and thus are no longer equivalent by symmetry after ionic relaxation. The average Fe–Fe bond length in the basal plane around a Fe^{3+} ion far from the polaron is 2.99 Å, with variations between 2.98 and 3.01 Å, so the Fe0–Fe2 and Fe0–Fe3 bond lengths do not differ significantly from the average, while the Fe0–Fe1 bond is shorter. The closest oxygen ions are significantly farther from the Fe^{2+} (all just over 2.0 Å) than the Fe^{3+} ions (all just under 2.0 Å) and these oxygen ion displacements can be seen in Figure 4.1 (C). In addition, the Fe^{2+} and the asymmetry of its nearest Fe neighbors is distinguished by calculated magnetic moments, as shown in Figure 4.1 (A). Comparison of magnetic moments from the literature can be found in the Results and Discussion.

Of the three nearest neighbor Fe^{3+} ions to the polaron on the Fe^{2+}, the Fe1 has a significantly smaller magnetic moment, $\mathbf{m}$, than the average magnetic moment of 4.17 μ_B and the other nearest neighbor Fe^{3+} ions, indicating that there is some charge density from the extra electron that is delocalized over this neighboring Fe. The polaron will hop to one of the nearest neighbor Fe^{3+} ions and we find, unexpectedly, a lower activation energy barrier and a higher electronic coupling for transport from Fe0 to Fe1 than to Fe2 (Table 4.2). We assume that the two Fe^{3+} that are 2.98 and 2.99 Å away from the Fe^{2+} will have similar activation energies since the difference between their distance and magnetic moments are insignificant, and only one such activation energy is explicitly calculated.

The asymmetry of the nearest neighbor Fe^{3+} ions is important to take into account when finding polaron trajectories through the crystal and is discussed in the Results and discussion section. The polaron will oscillate between the initial Fe0 and final Fe1 ions more easily than randomly diffusing in the basal plane. In the 30 atom hexagonal cell there are only two Fe ions represented on each basal plane, so there is no need to test different hop directions.

Once the linear interpolation between the initial and final polaron configurations is created, each image along the reaction coordinate is relaxed electronically. The adiabatic activation energy, $\Delta\tilde{G}_{\mathrm{ad}}$, from the linear interpolation and then ΔG_{ad} is derived from the refined saddle point, which is verified by performing subsequent phonon calculations.

4.2.3 Choice of U

In all calculations we made use of the rotationally invariant form of the LDA+U approach introduced by Dudarev et al.[51]. In this formalism, the Hubbard model parameters, U and J, are not independent, and the energy depends only on the parameter $\mathrm{U}_{\mathrm{effective}} = \mathrm{U} - \mathrm{J}$. In the text above and below we refer to the value of $\mathrm{U}_{\mathrm{effective}}$ simply as U and set J=1.

One practical difficulty with the DFT+U approach is the tendency for the system to converge to different metastable states corresponding to different orbital occupancies[104]. To treat this problem in the current work we employ a “ramping” approach and also perform calculations with different initial perturbations of the ionic positions, in order to check that we are converging to the lowest–energy orbital configurations. In our “ramping” approach, we start with converged ionic positions using a value of U=4.3 eV and increase or decrease U in a step–wise manner, using the new converged ionic positions to restart with each new U.

4.2.4 Electronic coupling

In previous applications of the DFT+U approach to calculating polaron activiation energies [73, 96, 97] it has been implicitly assumed that the hopping process is adiabatic. This assumption has been shown to be valid for the case of nearest–neighbor polaron transfer in α–Fe_2O_3 from previous wavefunction–based calculations[70, 71]. However, in cases where previous such calculations have not been performed it is useful to have a framework for checking the validity of the assumption of adiabatic processes within the DFT+U formalism. For this purpose we propose the following approach to computing the parameter V_{AB} required for the calculation of γ defined above.

We estimate the electronic coupling matrix element along the lines of the Mulliken–Hush formalism within Marcus Theory, as described in this reference[105]. Strictly speaking, the Mulliken–Hush formalism only applies when the TS wavefunction is a linear combination of the initial and final wavefunctions, such that these polaron wavefunctions can be thought of as atomic orbitals. The DOS (Figure 4.3) and charge density show that the extra electron is a small polaron with 'd'–orbital character in the ground state, as can been seen in Figs.4.1 (A) and (C). The highest occupied 'orbital' and lowest unoccupied 'orbital' at the TS also have localized 'd'–character, suggesting that they are the 'bonding' and 'antibonding' linear combinations of the ground state orbitals (bonding orbital shown in Figure 4.1 (B)). The character of these orbitals gives us confidence that we can use the Mulliken–Hush formalism to estimate V_{AB} from the TS electronic structure of hematite.

In the Mulliken–Hush formula, ΔE_{12} is the energy difference between the adiabatic bonding and antibonding electronic states at the transition point, as given below:

$$V_{AB} = \frac{1}{2}\Delta \mathrm{E}_{12}. \tag{4.3}$$

This energy difference will be estimated from the positions of the two defect states, above and below the Fermi energy, in the DOS calculated in the transition state, as shown in the Results and discussion section.

4.3 Results and discussion

This section starts by presenting the estimation of the mobility. Using U=4.3 eV, the value of the mobility is only a factor of two smaller than experiment. We next discuss our choice of U and describe the difference between using the relaxed saddle point versus the TS from the linear interpolation. Finally our estimation of the electronic coupling is presented.

4.3.1 Mobility

We validate the DFT+U method by comparison to the experimental mobility. The mobility, μ, as shown in Eqtn. 4.4, can be calculated from the rate of electron transfer, τ. Also in Eqtn. 4.4 is the relation between mobility and the diffusion coefficient, D. We use kT=

0.02499 eV as in the experimental measurement, and a is the electron transfer distance, where we use our average calculated nearest Fe–Fe distance of 2.99 Å.

$$\mu = \frac{eD}{kT} = \frac{e}{kT}\frac{a^2\tau}{2} \tag{4.4}$$

It is to be noted that in comparing the mobility to experiment, we will employ the value of τ for nearest–neighbor hopping to Fe1 in Eqtn. 4.4. This is an approximation because the τ is different for different neighbors, as described above, and is significantly lower for smaller for hopping along the c–axis than within the basal plane. Thus, our calculated mobilities should be viewed as an upper bound when compared to measurements on polycrystalline samples, which average over hop directions.

In the adiabatic limit, the rate of electron transfer is related to the attempt frequency – τ_0, the frequency of the mode that transfers the polarization of the lattice around the initial Fe to the final Fe and in Eqtn. 4.1, $A = N * \tau_0$, where N is the number of nearest neighbors. Since electron transfer in hematite is strongly in the adiabatic regime, we determine the attempt frequency by calculating the phonon modes at the initial and saddle configurations[106].

The classical attempt frequency is the ratio of the product of the vibrational modes at the ground and transition states (where all modes are populated) and we calculate it to be $\frac{\prod_{i=1}^{3N-3}\nu_0^{GS}}{\prod_{i=1}^{3N-4}\nu_0^{TS}} = 2.93$ THz. The products do not include the three translational modes and there is one fewer term in the denominator due to the additional unstable mode at the TS. However, the classical attempt frequency should not be used since it assumes the temperature is much higher than the Debye temperature of around 480K[107]. Since we are interested in comparing to experimental measurements at room temperature, we employ instead a calculation of the attempt frequency using the full quantum–mechanical expression for the vibrational free energy in the saddle and ground–state configurations, accounting for the temperature–dependent occupations of the phonon modes. This procedure, which is detailed in Ref. [108] and whose result is shown below, gives a much higher attempt frequency at room temperature of 60.4 THz.

$$\tau_0 = \frac{kT}{h}\exp\left(-\sum_{Re[m]}\ln\left[2\sinh\left(x_m^{TS}\right)\right] - \sum_{Re[m]}\ln\left[2\sinh\left(x_m^{GS}\right)\right]\right) \tag{4.5}$$

The phonon modes in the 30 atom unit cell are calculated for U=4.3 eV at the ground state and saddle–point. At the relaxed saddle point there is an unstable mode of $14.64\boldsymbol{i}$ THz ($488.33\boldsymbol{i}$ cm^{-1}). Calculation of the phonon modes of bulk hematite using VASP PAW–potentials has not yet been published, so we give our results from the rhombohedral cell

Table 4.2: Mobilities, activation energies, and the electronic coupling for polaron transport across two different paths to Fe1 and Fe2 show significant differences between the saddle point (center column) and linear interpolation (right column).

	μ [cm^2/(Vs)]	ΔG_{ad} [eV]	V_{AB}	$\tilde{\mu}$	$\Delta\tilde{G}_{\mathrm{ad}}$	$\tilde{\mathrm{V}}_{AB}$
experiment	0.04	0.118(2)				
U=4.3 Fe1	0.018	0.13	0.41	0.004	0.17	0.29
Fe2	0.008	0.15	0.35	0.0002	0.24	0.23
U=3.8 Fe1	0.29	0.06	0.40	0.088	0.09	0.30
Fe2	0.29	0.06	0.40	0.002	0.18	0.22
cluster[70]				0.00056	0.19	0.190
cluster[71]				0.062	0.11	0.204
nnn		0.33	0.014		0.34	0.012

in the Appendix.

Our calculation of the adiabatic activation energy using the relaxed saddle point and U=4.3 eV gives a mobility of 0.018 cm^2/(Vs), which compares favorably to the experimental value of 0.04 cm^2/(Vs)[72]. This calculated result is significantly higher than the value of 0.00056 cm^2/(Vs) derived by Iordanova et al. [70] using wavefunction–based cluster calculations. This discrepancy comes from the somewhat larger value for $\Delta\tilde{G}_{ad}$ in their calculations, which is comparable to what we compute by linear interpolation of the TS geometry, but 0.06 eV higher than that corresponding to the saddle point in our calculations. Additionally, the “attempt frequency” derived in Ref. [70] is estimated to be 90 THz, which is 31 times larger than the value calculated in this study. This larger prefactor, A, in Eqtn. 4.1, is estimated using $\frac{\mathrm{V}_{AB}^2}{\hbar}\left(\frac{1}{16\pi\Delta G_{\mathrm{dia}}kT}\right)^{\frac{1}{2}}$, which is a bastardization of the Marcus Theory formalism, since this prefactor is intended for non–adiabatic transfers that follow Fermi's golden rule.

4.3.2 Choice of U

An important question in the present DFT+U based approach to calculating polaron mobilities is the choice of the value of the effective Hubbard–U parameter. In order to test the dependence of our results on the value of U, we calculated the activation energy barrier from linear interpolation ($\Delta\tilde{G}_{\mathrm{ad}}$) for transfer to Fe1 and Fe2 in the 120 atom supercell with values of U from 3.1 to 6.3 eV, which cover the range of U values presented in literature for hematite[86, 99, 21], maghemite (γ–Fe$_2$O$_3$)[109], and magnetite[110, 111, 112, 113, 20, 114, 115, 116]. Since magnetite, Fe$_3$O$_4$, contains both Fe^{3+} and Fe^{2+} ions, the value of U found to be useful for modeling this material, which is typically smaller than those used for hematite, might be viewed as more appropriate for modeling electron polarons in α–F_2O_3.

Our results in Table 4.3 show there is a strong monotonic dependence of $\Delta\tilde{G}_{\mathrm{ad}}$ on the chosen value of U. The values of $\Delta\tilde{G}_{\mathrm{ad}}$ for transfer to Fe1 using values of U less than or equal to 3.8 eV are significantly smaller than those to Fe2, which can be understood because the polaron is more delocalized with smaller values of U and preferentially delocalizes over the Fe1 neighbor rather than over the other two nearest neighbors.

The appropriate value of U for a given system can be evaluated by comparing to experiment or higher levels of theory, such as hybrid functionals. By comparison of their calculated DOS to X-ray photoemission and inverse photoemission spectra, Rollmann et al. suggest setting U=4 eV[99]. Two calculations of hematite with hybrid functionals have been compared to DFT+U and suggest setting U to 4.3[86], a value which was calculated using linear response theory and unrestricted Hartree–Fock[117], or 4 eV[]. For magnetite, hybrid functionals calculation compared to DFT+U suggest U=3.8 eV[20].

Another measure of the soundness of a chosen U is the predicted magnetic moment of Fe. Experiment measures 4.6 μ_B[102], and our calculated value of 4.18 μ_B (in the bulk with U=4.3 eV) compares well to the HSE(with 12% exact exchange) calculation of 4.16 μ_B [21]. A recent paper, which aims to predict band gaps, found similar magnetic moments between hybrid functionals and DFT+U with U=4.3 eV[86] . Table 4.3 presents the average magnetic moment on the Fe ions involved in the electron transfer (labeled Fe^{2+}) and the average magnetic moment of all other Fe^{3+} ions in the cell at the TS for transfer between Fe0 and Fe1. Our results show that the for U=3.8, 4.0 and 4.3 eV, the magnetic moment on the two Fe ions involved in the polaron transfer at the TS does change significantly.

As mentioned above, U values between 3.8 and 4.3 eV compare well to the wavefunction–based methods using iron clusters. Setting U=4.3 eV, gives a $\Delta\tilde{G}_{\mathrm{ad}}$ for transfer to Fe1 of 0.17 eV, which compares very well to the more recent wavefuncton–based publication[70] result of 0.19 eV, though the result from U=4 eV compares well to the older publication by Rosso et al. [71]. Because our calculation of the relaxed saddle point activation energy of 0.13 eV using U=4.3 eV also compares well with experiment[72], we proceed with U=4.3 eV for estimating the mobility. In addition, we present results from the relaxed saddle point using U=3.8 eV, to demonstrate how a smaller value of U can change the electronic coupling due to increased delocalization of the polaron.

4.3.3 The saddle point and finite size effects

The linearly interpolated transition state is not the true saddle point, having forces up to 0.4 eV/Å on many of the ions in Fe_2O_3. Using the more refined saddle point structure lowers the calculated activation energy barrier by up to 0.1 eV for different polaron tra-

Table 4.3: The activation energy from the linear interpolation increases monotonically with increasing choice of U for polaron transport to both Fe1 and Fe2. The average magnetic moment at the TS, $\bar{\mathbf{m}}$ [102], is shown in order to compare to the experimental value of 4.6 μ_B, where the second to last column is the average of the magnetic moment on the initial and final Fe ions involved in the polaron transfer to Fe1 and the final column is the average of all the other Fe ions.

	$\Delta\tilde{G}_{\text{ad}}$ [eV]		$\bar{\mathbf{m}}$ [μ_B]	
U (eV)	Fe1	Fe2	Fe^{2+}	Fe^{3+}
3.1	0.01	0.13	3.85	4.07
3.3	0.03	0.15	3.86	4.08
3.8	0.09	0.18	3.91	4.13
4.0	0.12	0.20	3.93	4.15
4.3	0.17	0.24	3.95	4.18
5.3	0.32	0.35	4.02	4.26
6.3	0.47	0.51	4.09	4.35

jectories and values of U. Relaxing the TS brings the activation energy with U=4.3 eV closer to the experimental value of 0.118 eV[72], from 0.17 to 0.13 eV. The experimental adiabatic activation energy is measured in 3% Ti–doped Fe_2O_3, which our dilute limit calculation can simulate with the positive background charge compensating for the extra electron. Intentionally n–doping allows the experimental ΔG_{ad} to just measure the barrier to transport rather than including the formation energy of the charge carrier.

The above calculations with different values of U are calculated with a 120 atom supercell, but we also use the 30 atom supercell in order to test the finite size effects. The ground–state electronic structure differs significantly between the unit cell and supercell, as can be seen in the DOS from Figure 4.3, and indicates that finite size effects are significant. In the larger 120 atom supercell the initial and final Fe atoms are 7.8 Å across the periodic boundary, while in the 30 atom cell, the distance between the initial and final Fe ions is 2.95 Å, but these atoms are also 3.05 Å from each other across the periodic boundary (Figure 4.1 (C)). Thus we use calculation of the activation energy from the 120 supercell to compare to experiment. Even though finite size effects are significant in the electronic structure, the activation energy does not change much between the different sized cells, as described below. Since calculations of phonons in the supercells are insurmountably expensive, the unit cell is deemed adequate to estimate the attempt frequency.

The hexagonal unit cell of hematite predicts the same saddle point ΔG_{ad} of 0.15 eV (U=4.3 eV) as the polaron transfer to Fe2 in the 120 atom cell. The average of the $\Delta\tilde{G}_{\text{ad}}$ for polaron transfer to Fe1 and Fe2 (0.17 and 0.24 eV) for the 120 atom supercells gives about the same $\Delta\tilde{G}_{\text{ad}}$ as the 30 atom supercell, 0.20 eV, which seems reasonable. The similar activation

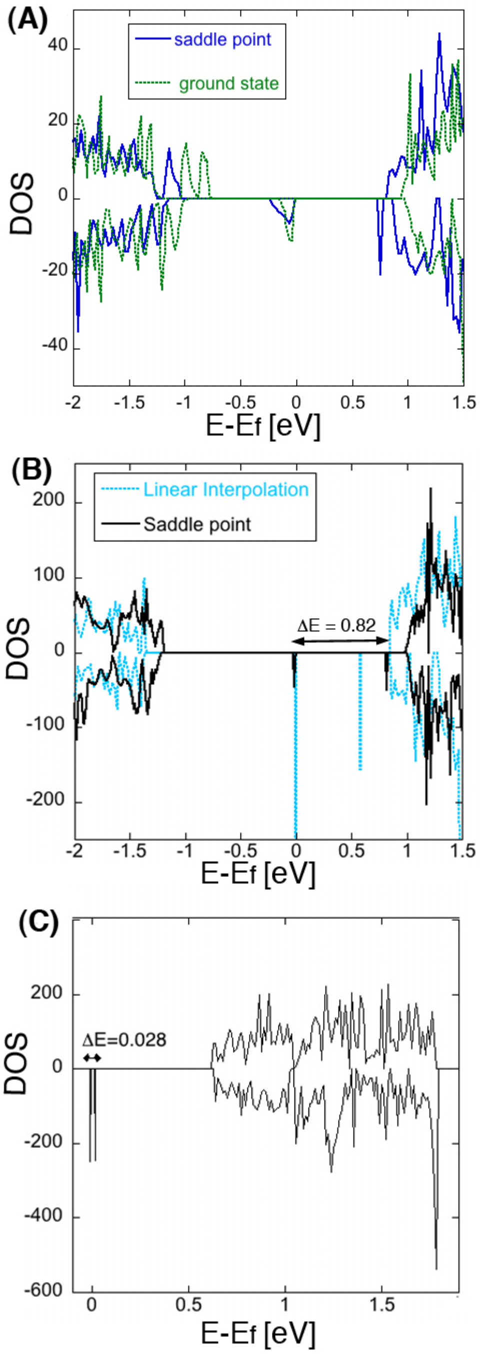

Figure 4.3: (A) The DOS for the hexagonal unit cell shows the narrow band due to the polaron in the ground state near the Fermi energy (E_f) in green. At the saddle point, the 'bonding' and 'antibonding' orbitals are both in the spin–down channel and show some broadening due to the periodic image (in blue). (B) The peaks due to the polaron sharpen in the 2x2x1 supercell compared to the unit cell for both the linear interpolation (light blue) and the saddle point (black). (C) The next nearest neighbor DOS shows two sharp peaks very close to the E_f, indicating very little electronic coupling.

energies between the 30 and 120 atom cells suggests that polarization of the lattice due to the polaron is confined to about a lattice vector.

4.3.4 Electronic coupling

The electronic coupling, V$_{AB}$, is well defined in the cluster–wavefunction based method and is related to S_{AB}, the overlap between the initial electronic wavefunction, ψ_A, and the final electronic wavefunction, ψ_B, at the transition state coordinate.

$$\begin{array}{rcl} V_{AB} & = & \frac{|H_{AB}-S_{AB}(H_{AA}+H_{BB})/2|}{1-S_{AB}^2} \\ H_{ij} & = & \langle\psi_i|H|\psi_j\rangle \\ S_{AB} & = & \langle\psi_A|\psi_B\rangle \end{array} \tag{4.6}$$

Rosso et al.[71] calculate $\tilde{\mathrm{V}}_{AB}$ to be 0.204 eV for the nearest neighbor electron transfer in the basal plane by calculating wavefunction overlap and Iordanova et al.[70] calculate V$_{AB}$ to be 0.190 eV using the Mulliken–Hush formula (Eqtn. 4.3). These values compare well to our estimation of the electronic coupling at the linear interpolated TS using the Mulliken–Hush formalism and U=3.8 and 4.3 eV as shown in Table 4.2.

We determine ΔE$_{12}$ from the DOS, for example in Figure 4.3 (B) for U=4.3 eV. Determining whether the Mulliken–Hush formula in Eqtn. 4.3 is appropriate in the DFT+U calculation of the electronic structure is discussed in the Methods section.

As expected, at the saddle point, the electronic coupling of V$_{AB}$=0.41 eV for Fe1 and 0.35 eV for Fe2 is stronger compared to the linear interpolated TS. Somewhat surprisingly, setting U=3.8 eV does not significantly change the estimate of the electronic coupling for transfer to Fe1 with U=4.3 eV (4.2). Furthermore, using the relaxed saddle point with U=3.8 eV gives equivalent values of the activation energy and the electronic coupling for transfer to Fe1 or Fe2, even though V$_{AB}$ differs with the linear interpolation. This is possibly due to increased ability of the polaron to delocalize with U=3.8 eV upon relaxation of the ionic positions. Unsurprisingly, all these calculations put the nearest neighbor electron transfer in the basal plane of hematite strongly is in the adiabatic regime.

We wanted to test the ability of this method to calculate transfer near the diabatic limit, so we looked at the next nearest neighbor (nnn) coupling. In Figure 4.1 (A), the next–nearest neighbor hop corresponds to transfer from the Fe0 ion to the Fe ion near the **b** lattice vector in the same basal plane, at a distance of approximately 5 Å. Using the nnn electronic structure at the saddle point in Figure 4.3 (C), we find V$_{AB}$=0.014 eV, which is smaller that the value estimated by Rosso et al. of $\tilde{\mathrm{V}}_{AB}$=0.06 eV[71], but still on the cusp of the adiabatic and diabatic regime. Thus, we conclude that DFT+U can also determine the adiabaticity of polaron transfer.

4.4 Summary

We show that calculating the mobility, adiabatic activation energy, and electronic coupling for polarons on metal ions with DFT+U is a viable method since it compares favorably with experiment and the cluster–wavefunction based method. The two wavefunction–based calculations[70, 71], of $\Delta\tilde{G}_{\text{ad}}$ in hematite employ a linear interpolation to determine the transition state coordinates, but we show that using the relaxed saddle–point coordinates gives a better description of electron–phonon coupling that is closer to the experimental measurement of electron mobility in hematite. Using the value of U=4.3 eV is adequate for predicting activation energy barriers and electronic coupling, especially since values of U close to 4.3 eV do not change the electronic coupling or ΔG_{ad} by much.

Finally, we find it is possible to predict the adiabatic versus diabatic regime of electron transfer in hematite using the electronic structure (DOS) at the saddle point. The agreement between the DFT+U and wavefunction–based calculations and experiment gives us confidence that this method can be used to predict polaron transport properties in new materials and help materials design for technological applications.

4.5 Appendix/Supplementary Material

4.5.1 Phonons in bulk hematite

We performed bulk phonon calculations on the rhombohedral primitive cell to help inform our calculations of the 30 atom hexagonal cell with the extra localized electron. There have been two publications of the phonon modes of hematite, the first by Chamritski et al.[118] using interatomic Buckingham potentials and the second by Blanchard et al.[119] using DFT+U as implemented in PWSCF. We chose to report our VASP results since they differ slightly from the PWSCF calculation. We agree on all peak assignments except for the two italicized lines in Table I of the Appendix. Blanchard et al. assigns the experimental peak[120, 121, 122] at 297 cm^{-1} as a E_g mode, but we assign it as E_u (as did Chamritski) by matching the VASP determined atom displacements with the theoretical phonon mode displacements as calculated by SMODES and ISOTROPY (free online software by H. T. Stokes and D. M. Hatch). While Blanchard et al. assign the peak at 243 cm^{-1} as the E_u mode, we and Chamritski (using IR and Raman spectroscopy[123, 124]) find it to be of E_g character.

4.5.2 Phonons at the transition point

Phonon calculations in the 30 atom unit cell with U=4.3 eV are calculated at the ground state (GS) and saddle point (TS) in order to calculate the attempt frequency, τ_0. First the GS is given and then the TS with the imaginary mode in italics.

GS phonon modes in meV:

75.361236, 74.488224, 73.647842, 73.595373, 73.180261, 68.374181, 67.381748, 66.473775, 65.202875, 65.115274, 64.726036, 64.569645, 64.406384, 63.294114, 60.908155, 60.439803, 60.301328, 59.425207. 59.012777, 58.899947, 56.701297, 56.679626, 55.099485, 55.006942, 50.141569, 48.431265, 48.113792, 47.844257, 47.576271, 47.189781, 46.839747, 46.331033, 45.668740, 45.575850, 44.717222, 44.566958, 44.523005, 44.145705, 43.914829, 43.808481, 43.170045, 40.401246, 37.992240, 37.644922, 37.412568, 37.011380, 35.950282, 35.835343, 35.495915, 34.965467, 34.746269, 34.637623, 34.537935, 34.282331, 33.958044, 33.923401, 33.374745, 33.136965, 33.015018, 32.813694, 32.641412, 32.124432, 32.092973, 31.505421, 31.046427, 30.722320, 30.230126, 27.545653, 26.464855, 25.800482, 25.653737, 25.197013, 23.951552, 23.212738, 20.331350, 19.934667, 19.857384, 19.727659, 19.433095, 19.253468, 18.830060, 18.688827, 18.231385, 10.935317, 10.769033, 10.521213, 9.846469, 0.165858, 0.192157, 0.243812

TS phonon modes in meV:

87.474920, 74.948556, 74.828633, 73.881718, 73.717062, 73.372077, 68.111364, 67.094035, 65.535375, 65.400860, 65.079523, 64.728271, 64.420090, 64.138102, 61.917920, 61.190364, 60.581678, 60.410040, 59.894597, 59.301826, 59.169759, 57.054449, 56.836459, 55.536715, 49.691357, 48.598462, 48.148659, 47.978682, 47.773351, 47.416614, 46.689696, 46.297717, 45.777230, 45.567671, 45.283289, 44.931335, 44.811107, 44.511628, 44.277000, 43.412135, 40.648553, 38.887241, 38.359402, 37.663771, 37.337848, 37.091440, 36.369950, 36.012624, 35.591272, 35.347844, 35.194832, 34.690229, 34.502296, 34.390444, 34.255382, 34.052806, 33.347499, 32.955512, 32.909120, 32.772699, 32.493596, 32.300570, 31.861741, 31.641705, 30.818153, 29.594393, 28.711370, 27.566440, 26.240321, 25.575396, 25.228488, 23.748146, 23.400776, 20.557989, 20.321415, 20.132345, 20.061547, 19.810094, 19.253439, 19.187090, 18.797337, 18.332946, 13.011216, 10.982415, 10.774474, 10.589071, 4.671390, 0.814117, 1.571635, *60.545218*

4.5.3 Symmetry operations for final configuration

In section 4.2.2, a general function was given to transfer the initial ion coordinates to the final ion coordinates. Here, I provide a short bash script that helps to streamline this process for the 2x2x1 supercell nearest neighbor transfer. In order to run the script (which I called `awkscript16`), a POSCAR file with only the coordinates is needed. After the VASP header with the lattice coordinates must be added back in. Usually I copy the CONTCAR to the coordinates only file ‘cont’ and then run the script from the unix command line as follows: `awkscript16 cont`

```
 #!/bin/sh
awk ‘{print $0,NR >> "temp"}’ $1
awk ‘{
if (1/6 - $1 <= 0) $1 = 7/6-$1;
else $1 = 1/6 - $1;
if (-$2+5/6 <= 0) $2 = 11/6-$2;
else $2 = 5/6 - $2;
if (-$3+2/3 <= 0) $3 = 5/3-$3;
else $3 = 2/3 - $3;
printf ‘‘%1.16f %1.16f %1.16f %1.0f \n", $1, $2, $3, $4 >> "tempcont" }’ temp
paste numfile2 tempcont | sort -n > "tempcont2"
awk ’{printf "%1.16f %1.16f %1.16f \n", $2, $3, $4 >> "cont02" }’ tempcont2
rm temp*
```

Table 4.4: Phonon modes from the bulk rhombohedral primitive cell use U=4.3 eV. The previous calculations of phonons in hematite assign their peaks using different experimental IR and Raman measurements, so we report the experimental values from both in the columns 3 and 4.

Calc. ν[cm^{-1}]	Symm.	Ref[118] Exp[123, 124]	Ref[119] Exp[120, 121, 122]
622.7	$\mathrm{A_{2g}}$		
552.7	$\mathrm{E_g}$	613	609
537	$\mathrm{A_{1u}}$		
476.4	$\mathrm{A_{2u}}$		
442.5	$\mathrm{A_{1g}}$	498	496
396.4	$\mathrm{A_{2g}}$		
376.4	$\mathrm{E_u}$	380–400	433–437
387.8	$\mathrm{E_g}$	412	408
317.5	$\mathrm{A_{1u}}$		
271.5	E_u	310–335	297
226	$\mathrm{A_{2u}}$	310–335	299–301
270.5	$\mathrm{E_g}$	299	290
261	E_g	293	286–292
207.5	$\mathrm{E_g}$	247	243
217.4	$\mathrm{E_u}$	229	216–227
199.5	$\mathrm{A_{1g}}$	225	224
167.4	$\mathrm{A_{2g}}$		

Chapter 5

Conclusions and future work

The studies presented in this thesis, both computational and experimental, have greatly increased our knowledge of proton and polaron conductivity in insulators. The main findings from each chapter are as follows.

Chapter 2: We find that the binding energy of protons to Ba–dopants in $LaPO_4$ is 0.2 eV and is mainly due to electrostatic interactions. This binding energy can be used to explain the increased activation energy for proton transport upon doping.

Chapter 3: The electronic structure of $CePO_4$ is calculated with DFT+U and compares well to X–ray spectroscopy when U is set to 3 eV with the LDA functional. The density of states show that holes sitting on Ce cations are favorable since the lone Ce '4f' electron is the closest to the Fermi energy.

Chapter 4: We developed a DFT+U method for calculating small–polaron mobility in hematite; our results compare favorably with experiment and wavefunction–based methods. Furthermore, we can estimate the electronic coupling matrix element from the DOS, which puts the polaron transfer strongly in the adiabatic regime (as is also predicted by cluster/wavefunction based methods).

Unpublished AC and DC impedance measurements of solid solutions of $LaPO_4$ and $CePO_4$ show that substituting Ce on La sites dramatically increases the power of $Ce_xLa_{1-x}PO_4$ in a fuel cell set-up (manuscript in preparation by H. L. Ray and L. C. De Jonghe). Ce/La orthophosphate solutions with increased power output could compete with current commercial proton-conducting materials, so future computational and experimental work on rare-earth phosphates should focus on understanding mixed conductivity in these materials. The effect of Ce_{La} seems to be a lower activation energy for proton transport, which we have shown can be calculated with density functional theory in lanthanum orthophosphate.

The work presented in this thesis provides a strong foundation to design computational experiments to test the effect of Ce/La solutions on the carrier concentration, n, and mobility, μ. Through investigation of $LaPO_4$, we showed that Ba-dopants bind protons by 0.2 eV in 2x2x2 supercells, primarily due to electrostatic interactions. Subsequent investigations show that Sr-dopants bind protons by even more - 0.3 eV in 3x3x3 supercells. One hypothesis for the increase in power of Ce/La solid solutions is that hole-polarons, stable due to the Ce cations, can compete with the protons for 'binding' with the dopants, thus decreasing the activation energy for proton transport through the material. Future studies similar to those demonstrated above for the of the electronic structure of doped and undoped $CePO_4$ and polaron transport in hematite would be helpful to inform future investigations into mixed hole/proton conductivity in Ce/La solid solutions.

The DFT+U $CePO_4$ electronic structure shows a sharp peak at the Fermi energy with Ce 'f' character, which can be easily oxidized to Ce^{4+}, potentially creating a small-polaron. Unpublished work on Sr-doped $CePO_4$ shows that the hole can indeed sit on the Ce ions, as demonstrated in the last section of Chapter 3. While we would like to calculate the activation energy for polaron hopping in $CePO_4$, magnetic frustration and difficulty with electronic convergence have led us to design some simpler calculations.

By moving the lone Ce^{3+} '4f' electron into the core with the Ce3 pseudopotential available with VASP, the Hubbard U is no longer needed to localize the electron and calculations converge more easily. To start, we wanted to know how strongly the hole versus the proton binds to Sr-dopants in $CePO_4$. The hole is created by replacing on Ce3 pseudopotential with a regular Ce pseudopotential and then the number of electrons near that rare-earth site is reduced due to the Sr-dopant. Further work should involve creating Ce/La solid solutions and determining the change in the proton's activation energy barrier in the presence of hole-polarons.

The mystery of why the concentration of protons is significantly smaller than the concentration of dopants still remains for rare-earth phosphates. Thermodynamic models of defect concentrations may shed light on the number of carriers in $LaPO_4$, $CePO_4$ and their solid solutions and whether substituting Ce for La increases the proton concentration in these materials. Equations 1.7 and 1.6 are the basis for the thermodynamic models of defect concentrations. The chemical potential of the reactants and products are equal, as shown below and explained in Ref. [11]. The chemical potentials can be related to the Helmholtz free energy that is calculated with DFT and the equilibrium constant can be determined at different temperatures and gas pressures (since the chemical potential of water, for example, depends strongly on T and P).

$$\mu_{\mathrm{P_2O_7^{\bullet\bullet}}} + \mu_{\mathrm{H_2O}} = \mu_{\mathrm{2HPO_4^{\bullet}}} \tag{5.1}$$

Knowledge of defect concentrations at different oxygen and water partial pressures will help interpretation of AC and DC conductivity data, as presented in Figure 1.2.

Bibliography

[1] *America Creating Opportunities to Meaningfully Promote Excellence in Technology, Education, and Science Act*, vol. 20, no. HR 2272.

[2] T. Norby, "The promise of protonics," *Nature*, vol. 410, no. 6831, pp. 877–878, 2001.

[3] T. E. Springer, T. A. Zawodzinski, and S. Gottesfeld, "Polymer electrolyte fuel-cell model," *Journal of the Electrochemical Society*, vol. 138, no. 8, pp. 2334–2342, 1991.

[4] K. D. Kreuer, "Aspects of the formation and mobility of protonic charge carriers and the stability of perovskite-type oxides," *Solid State Ionics*, vol. 125, no. 1-4, pp. 285–302, 1999.

[5] D. T. Chin and H. H. Chang, "On the conductivity of phosphoric-acid electrolyte," *Journal of Applied Electrochemistry*, vol. 19, no. 1, pp. 95–99, 1989.

[6] I. S. Cho, G. K. Choi, J. S. An, J. R. Kim, and K. S. Hong, "Sintering, microstructure and microwave dielectric properties of rare earth orthophosphates, repo4 (re = la, ce, nd, sm, tb, dy, y, yb)," *Materials Research Bulletin*, vol. 44, no. 1, pp. 173–178, 2009.

[7] Y. X. Ni, J. M. Hughes, and A. N. Mariano, "Crystal-chemistry of the monazite and xenotime structures," *American Mineralogist*, vol. 80, no. 1-2, pp. 21–26, 1995.

[8] N. Kitamura, K. Amezawa, Y. Tomii, T. Hanada, N. Yamamoto, T. Omata, and S. Otsuka-Yao-Matsuo, "Electrical conduction properties of sr-doped lapo4 and cepo4 under oxidizing and reducing conditions," *Journal of the Electrochemical Society*, vol. 152, no. 4, pp. A658–A663, 2005.

[9] R. Yu and L. C. De Jonghe, "Proton-transfer mechanism in lapo4," *Journal of Physical Chemistry C*, vol. 111, no. 29, pp. 11003–11007, 2007.

[10] G. Harley, R. Yu, and L. C. De Jonghe, "Proton transport paths in lanthanum phosphate electrolytes," *Solid State Ionics*, vol. 178, no. 11-12, pp. 769–773, 2007.

[11] J. Solomon, N. Adelstein, M. Asta, and L. C. De Jonghe, "Charge-compensating pyrophosphate defect structures in sr-doped lapo4," *Electrochemical Society Transactions*, 2012.

[12] G. C. Mather, C. A. J. Fisher, and M. S. Islam, "Defects, dopants, and protons in lanbo4," *Chemistry of Materials*, vol. 22, no. 21, pp. 5912–5917, 2010.

[13] P. L. Freddolino, A. S. Arkhipov, S. B. Larson, A. McPherson, and K. Schulten, "Molecular dynamics simulations of the complete satellite tobacco mosaic virus," *Structure*, vol. 14, no. 3, pp. 437–449, 2006.

[14] R. Martin, *Electronic Structure: Basic Theory and Pratical Methods.* Cambridge, UK: Cambridge Unniversity Press, 2004.

[15] P. Hohenberg and W. Kohn, "Inhomogeneous electron gas," *Physical Review B*, vol. 136, no. 3B, p. B864, 1964.

[16] W. Kohn and L. J. Sham, "Self-consistent equations including exchange and correlation effects," *Physical Review*, vol. 140, no. 4A, p. 1133, 1965.

[17] J. P. Perdew, K. Burke, and M. Ernzerhof, "Generalized gradient approximation made simple," *Physical Review Letters*, vol. 77, no. 18, pp. 3865–3868, 1996.

[18] V. I. Anisimov, F. Aryasetiawan, and A. I. Lichtenstein, "First-principles calculations of the electronic structure and spectra of strongly correlated systems: The lda+u method," *Journal of Physics-Condensed Matter*, vol. 9, no. 4, pp. 767–808, 1997.

[19] J. Heyd and G. E. Scuseria, "Efficient hybrid density functional calculations in solids: Assessment of the heyd-scuseria-ernzerhof screened coulomb hybrid functional," *Journal of Chemical Physics*, vol. 121, no. 3, pp. 1187–1192, 2004.

[20] A. D. Rowan, C. H. Patterson, and L. V. Gasparov, "Hybrid density functional theory applied to magnetite: Crystal structure, charge order, and phonons," *Physical Review B*, vol. 79, no. 20, 2009.

[21] Z. D. Pozun and G. Henkelman, "Hybrid density functional theory band structure engineering in hematite," *Journal of Chemical Physics*, vol. 134, no. 22, 2011.

[22] J. L. F. Da Silva, M. V. Ganduglia-Pirovano, J. Sauer, V. Bayer, and G. Kresse, "Hybrid functionals applied to rare-earth oxides: The example of ceria," *Physical Review B*, vol. 75, no. 4, 2007.

[23] V. I. Anisimov and O. Gunnarsson, "Density-functional calculation of effective coulomb interactions in metals," *Physical Review B*, vol. 43, no. 10, pp. 7570–7574, 1991.

[24] G. Henkelman, B. P. Uberuaga, and H. Jonsson, "A climbing image nudged elastic band method for finding saddle points and minimum energy paths," *Journal of Chemical Physics*, vol. 113, no. 22, pp. 9901–9904, 2000.

[25] R. A. Olsen, G. J. Kroes, G. Henkelman, A. Arnaldsson, and H. Jonsson, "Comparison of methods for finding saddle points without knowledge of the final states," *Journal of Chemical Physics*, vol. 121, no. 20, pp. 9776–9792, 2004.

[26] K. Amezawa, T. Tomiga, N. Yamamoto, T. Hanada, and Y. Tomii, "Electrical conduction properties of lap3o9 glass and glass-ceramics," *Journal of the American Ceramic Society*, vol. 88, no. 11, pp. 3211–3214, 2005.

[27] K. Amezawa, Y. Kitajima, Y. Tomii, N. Yamamoto, M. Wideroe, and T. Norby, "Protonic conduction in acceptor-doped lap3o9," *Solid State Ionics*, vol. 176, no. 39-40, pp. 2867–2870, 2005.

[28] K. Amezawa, Y. Uchimoto, and Y. Tomii, "High temperature protonic conduction in sr-doped lap3o9," *Solid State Ionics*, vol. 177, no. 26-32, pp. 2407–2411, 2006.

[29] N. Kitamura, K. Amezawa, Y. Uchimoto, Y. Tomii, T. Hanada, and N. Yamamoto, "Electrical conduction properties of rare earth orthophosphates under reducing conditions," *Solid State Ionics*, vol. 177, no. 26-32, pp. 2369–2373, 2006.

[30] G. Harley, K. D. Kreuer, J. Maier, and L. C. De Jonghe, "Structural investigation of ternary la/alkaline earth phosphate (la(1-x)mxp3oy) (m = ba, ca, sr) glasses," *Journal of Non-Crystalline Solids*, vol. 355, no. 16-17, pp. 932–937, 2009.

[31] J. Feng, "Nmr of proton - ba interaction," *Private Communication*, 2011.

[32] M. Karlsson, P. Fouquet, I. Ahmed, and M. Maccarini, "Dopant concentration and short-range structure dependence of diffusional proton dynamics in hydrated bainxzr1-xo3-x/2 (x=0.10 and 0.50)," *Journal of Physical Chemistry C*, vol. 114, no. 7, pp. 3292–3296, 2010.

[33] S. J. Stokes and M. S. Islam, "Defect chemistry and proton-dopant association in bazro3 and bapro3," *Journal of Materials Chemistry*, vol. 20, no. 30, pp. 6258–6264, 2010.

[34] F. Giannici, A. Longo, K. D. Kreuer, A. Balerna, and A. Martorana, "Dopants and defects: Local structure and dynamics in barium cerates and zirconates," *Solid State Ionics*, vol. 181, no. 3-4, pp. 122–125, 2010.

[35] M. S. Islam, "Ionic transport in abo(3) perovskite oxides: a computer modelling tour," *Journal of Materials Chemistry*, vol. 10, no. 5, pp. 1027–1038, 2000.

[36] M. E. Bjorketun, P. G. Sundell, and G. Wahnstrom, "Effect of acceptor dopants on the proton mobility in bazro3: A density functional investigation," *Physical Review B*, vol. 76, no. 5, 2007.

[37] L. Buannic, F. Blanc, I. Hung, Z. H. Gan, and C. P. Grey, "Probing the local structures and protonic conduction pathways in scandium substituted bazro3 by multinuclear solid-state nmr spectroscopy," *Journal of Materials Chemistry*, vol. 20, no. 30, pp. 6322–6332, 2010.

[38] G. Harley and L. C. De Jonghe, "Proton transport in doped la-metaphosphate glasses," *Solid State Ionics*, vol. 181, no. 8-10, pp. 424–429, 2010.

[39] K. D. Kreuer, "Proton-conducting oxides," *Annual Review of Materials Research*, vol. 33, pp. 333–359, 2003.

[40] D. A. Andersson, S. I. Simak, N. V. Skorodumova, I. A. Abrikosov, and B. Johansson, "Optimization of ionic conductivity in doped ceria," *Proceedings of the National Academy of Sciences of the United States of America*, vol. 103, no. 10, pp. 3518–3521, 2006.

[41] G. Kresse and J. Furthmuller, "Efficiency of ab-initio total energy calculations for metals and semiconductors using a plane-wave basis set," *Computational Materials Science*, vol. 6, no. 1, pp. 15–50, 1996.

[42] G. Kresse and J. Furthmuller, "Efficient iterative schemes for ab initio total-energy calculations using a plane-wave basis set," *Physical Review B*, vol. 54, no. 16, pp. 11169–11186, 1996.

[43] P. E. Blochl, "Projector augmented-wave method," *Physical Review B*, vol. 50, no. 24, pp. 17953–17979, 1994.

[44] H. J. Monkhorst and J. D. Pack, "Special points for brillouin-zone integrations," *Physical Review B*, vol. 13, no. 12, pp. 5188–5192, 1976.

[45] E. G. del Moral, D. P. Fagg, E. Chinarro, J. C. C. Abrantes, J. R. Jurado, and G. C. Mather, "Impedance analysis of sr-substituted cepo4 with mixed protonic and p-type electronic conduction," *Ceramics International*, vol. 35, no. 4, pp. 1481–1486, 2009.

[46] F. Zhou, K. S. Kang, T. Maxisch, G. Ceder, and D. Morgan, "The electronic structure and band gap of lifepo4 and limnpo4," *Solid State Communications*, vol. 132, no. 3-4, pp. 181–186, 2004.

[47] S. Fabris, S. de Gironcoli, S. Baroni, G. Vicario, and G. Balducci, "Taming multiple valency with density functionals: A case study of defective ceria," *Physical Review B*, vol. 71, no. 4, 2005.

[48] J. Kullgren, C. W. M. Castleton, C. Muller, D. M. Ramo, and K. Hermansson, "B3lyp calculations of cerium oxides," *Journal of Chemical Physics*, vol. 132, no. 5, 2010.

[49] G. Pacchioni, "Modeling doped and defective oxides in catalysis with density functional theory methods: Room for improvements," *Journal of Chemical Physics*, vol. 128, no. 18, 2008.

[50] K. Terakura, T. Oguchi, A. R. Williams, and J. Kubler, "Band theory of insulating transition-metal monoxides - band-structure calculations," *Physical Review B*, vol. 30, no. 8, pp. 4734–4747, 1984.

[51] S. L. Dudarev, G. A. Botton, S. Y. Savrasov, Z. Szotek, W. M. Temmerman, and A. P. Sutton, "Electronic structure and elastic properties of strongly correlated metal oxides from first principles: Lsda+u, sic-lsda and eels study of uo2 and nio," *Physica Status Solidi a-Applications and Materials Science*, vol. 166, no. 1, pp. 429–443, 1998.

[52] A. I. Lichtenstein and M. I. Katsnelson, "Ab initio calculations of quasiparticle band structure in correlated systems: Lda++ approach," *Physical Review B*, vol. 57, no. 12, pp. 6884–6895, 1998.

[53] A. I. Liechtenstein, V. P. Antropov, and B. N. Harmon, "Electronic-structure and magnetooptical effects in cesb," *Physical Review B*, vol. 49, no. 15, pp. 10770–10773, 1994.

[54] C. Sevik and T. Cagin, "Mechanical and electronic properties of ceo2, tho2, and (ce,th)o-2 alloys," *Physical Review B*, vol. 80, no. 1, 2009.

[55] Y. Jiang, J. B. Adams, and M. van Schilfgaarde, "Density-functional calculation of ceo2 surfaces and prediction of effects of oxygen partial pressure and temperature on stabilities," *Journal of Chemical Physics*, vol. 123, no. 6, 2005.

[56] M. Cococcioni and S. de Gironcoli, "Linear response approach to the calculation of the effective interaction parameters in the lda+u method," *Physical Review B*, vol. 71, no. 3, 2005.

[57] B. Glorieux, R. Berjoan, M. Matecki, A. Kammouni, and D. Perarnau, "Xps analyses of lanthanides phosphates," *Applied Surface Science*, vol. 253, no. 6, pp. 3349–3359, 2007.

[58] M. Repoux, "Comparison of background removal methods for xps," *Surface and Interface Analysis*, vol. 18, no. 7, pp. 567–570, 1992.

[59] G. Kresse and J. Hafner, "Abinitio molecular-dynamics for liquid-metals," *Physical Review B*, vol. 47, p. 558, 1993.

[60] C. Adamo and V. Barone, “Toward reliable density functional methods without adjustable parameters: The pbe0 model,” *Journal of Chemical Physics*, vol. 110, no. 13, pp. 6158–6170, 1999.

[61] G. W. Beall, L. A. Boatner, D. F. Mullica, and W. O. Milligan, “The structure of cerium ortho-phosphate, a synthetic analog of monazite,” *Journal of Inorganic & Nuclear Chemistry*, vol. 43, no. 1, pp. 101–105, 1981.

[62] F. D. Srygley and L. K. Wilson, “Crystalline structure and magnetic properties of monoclinic cepo4,” *Bulletin of the American Chemical Society*, vol. 24, no. 2, 1979.

[63] M. S. Hybertsen and S. G. Louie, “Spin-orbit-splitting in semiconductors and insulators from the abinitio pseudopotential,” *Physical Review B*, vol. 34, no. 4, pp. 2920–2922, 1986.

[64] M. Shishkin, M. Marsman, and G. Kresse, “Accurate quasiparticle spectra from self-consistent gw calculations with vertex corrections,” *Physical Review Letters*, vol. 99, no. 24, 2007.

[65] A. Fujimori, “Correlation-effects in the electronic-structure and photoemission spectra of mixed-valence cerium compounds,” *Physical Review B*, vol. 28, no. 8, pp. 4489–4499, 1983.

[66] D. Hobbs, G. Kresse, and J. Hafner, “Fully unconstrained noncollinear magnetism within the projector augmented-wave method,” *Physical Review B*, vol. 62, no. 17, pp. 11556–11570, 2000.

[67] M. Marsman and J. Hafner, “Broken symmetries in the crystalline and magnetic structures of gamma-iron,” *Physical Review B*, vol. 66, no. 22, 2002.

[68] K. Klier, P. Novak, A. C. Miller, J. A. Spirko, and M. K. Hatalis, “Electronic structure of cef3 and tbf3 by valence-band xps and theory,” *Journal of Physics and Chemistry of Solids*, vol. 70, no. 9, pp. 1302–1311, 2009.

[69] J. Paier, M. Marsman, and G. Kresse, “Why does the b3lyp hybrid functional fail for metals?,” *Journal of Chemical Physics*, vol. 127, no. 2, 2007.

[70] N. Iordanova, M. Dupuis, and K. M. Rosso, “Charge transport in metal oxides: A theoretical study of hematite alpha-fe2o3,” *Journal of Chemical Physics*, vol. 122, no. 14, 2005.

[71] K. M. Rosso, D. M. A. Smith, and M. Dupuis, “An ab initio model of electron transport in hematite (alpha-fe2o3) basal planes,” *Journal of Chemical Physics*, vol. 118, no. 14, pp. 6455–6466, 2003.

[72] B. Zhao, T. C. Kaspar, T. C. Droubay, J. McCloy, M. E. Bowden, V. Shutthanandan, S. M. Heald, and S. A. Chambers, "Electrical transport properties of ti-doped fe2o3(0001) epitaxial films," *Physical Review B*, vol. 84, no. 24, 2011.

[73] T. Maxisch, F. Zhou, and G. Ceder, "Ab initio study of the migration of small polarons in olivine lixfepo4 and their association with lithium ions and vacancies," *Physical Review B*, vol. 73, no. 10, 2006.

[74] H. Kakemoto, Y. Makita, Y. Kino, S. Sakuragi, and T. Tsukamoto, "Small polaron of -fesi2 obtained from optical measurements," *Thin Solid Films*, vol. 381, no. 2, pp. 251–255, 2001.

[75] H. Ishii, K. Honma, N. Kobayashi, and K. Hirose, "Wave-packet approach to transport properties of carrier coupled with intermolecular and intramolecular vibrations of organic semiconductors," *Physical Review B*, vol. 85, no. 24, 2012.

[76] O. F. Schirmer, M. Imlau, and C. Merschjann, "Bulk photovoltaic effect of linbo3:fe and its small-polaron-based microscopic interpretation," *Physical Review B*, vol. 83, no. 16, 2011.

[77] E. Thimsen, F. Le Formal, M. Gratzel, and S. C. Warren, "Influence of plasmonic au nanoparticles on the photoactivity of fe2o3 electrodes for water splitting," *Nano Letters*, vol. 11, no. 1, pp. 35–43, 2011.

[78] A. Yildiz, S. B. Lisesivdin, M. Kasap, and D. Mardare, "Non-adiabatic small polaron hopping conduction in nb-doped tio2 thin film," *Physica B: Condensed Matter*, vol. 404, no. 811, pp. 1423–1426, 2009.

[79] S.-F. Wang, Y.-F. Hsu, H.-C. Lu, C.-C. Huang, and C.-T. Yeh, "Sr1xprxco0.95sn0.05o3 ceramic as a cathode material for intermediate-temperature solid oxide fuel cells," *International Journal of Hydrogen Energy*, vol. 37, no. 17, pp. 12548–12556, 2012.

[80] Z.-Y. Tian, P. H. Tchoua Ngamou, V. Vannier, K. Kohse-Hoinghaus, and N. Bahlawane, "Catalytic oxidation of vocs over mixed co-mn oxides," *Applied Catalysis B: Environmental*, vol. 117-118, no. 0, pp. 125–134, 2012.

[81] K. M. Rosso and M. Dupuis, "Electron transfer in environmental systems: a frontier for theoretical chemistry," *Theoretical Chemistry Accounts*, vol. 116, no. 1-3, pp. 124–136, 2006.

[82] J. Katz, X. Zhang, K. Attenkofer, C. K., C. Frandsen, P. Zarzycki, K. Rosso, R. Falcone, G. Waychunas, and B. Gilbert, "Electron small polarons and their mobility in iron (oxyhydr)oxide nanoparticles," *Science*, vol. 337, no. 6099, 2012.

[83] P. L. Liao, M. C. Toroker, and E. A. Carter, "Electron transport in pure and doped hematite," *Nano Letters*, vol. 11, pp. 1775–1781, 2011.

[84] R. A. Marcus, "On the theory of oxidation-reduction reactions involving electron transfer .1," *Journal of Chemical Physics*, vol. 24, no. 5, pp. 966–978, 1956.

[85] M. D. Newton, "Electron transfer: Theoretical models and computational implementation," in *Electron Transfer in Chemistry, Volume 1: Principles, Theories, Methods, and Techniques* (V. Balzani, ed.), vol. 1, Weinheim, Federal Republic of Germany: Wiley-VCH, 2001.

[86] P. L. Liao and E. A. Carter, "Testing variations of the gw approximation on strongly correlated transition metal oxides: hematite (alpha-fe(2)o(3)) as a benchmark," *Physical Chemistry Chemical Physics*, vol. 13, no. 33, pp. 15189–15199, 2011.

[87] S. Kerisit and K. M. Rosso, "Kinetic monte carlo model of charge transport in hematite (-fe[sub 2]o[sub 3])," *J. Chem. Phys.*, vol. 127, p. 124706, Jan 2007.

[88] S. Kerisit, K. M. Rosso, Z. Yang, and J. Liu, "Dynamics of coupled lithium/electron diffusion in tio2 polymorphs," *Journal of Physical Chemistry C*, vol. 113, pp. 20998–21007, 2009.

[89] S. Kerisit and K. M. Rosso, "Kinetic monte carlo model of charge transport in hematite (-fe[sub 2]o[sub 3])," *J. Chem. Phys.*, vol. 127, p. 124706, Jan 2007.

[90] F. N. Skomurski, S. Kerisit, and K. M. Rosso, "Structure, charge distribution, and electron hopping dynamics in magnetite (fe3o4) (100) surfaces from first principles," *Geochimica et Cosmochimica Acta*, vol. 74, pp. 4234–4248, Aug 2010.

[91] E. Artacho, D. Sanchez-Portal, P. Ordejon, A. Garcia, and J. M. Soler, "Linear-scaling ab-initio calculations for large and complex systems," *Physica Status Solidi B-Basic Solid State Physics*, vol. 215, no. 1, pp. 809–817, 1999.

[92] T. Van Voorhis, T. Kowalczyk, B. Kaduk, L. P. Wang, C. L. Cheng, and Q. Wu, "The diabatic picture of electron transfer, reaction barriers, and molecular dynamics," in *Annual Review of Physical Chemistry, Vol 61* (S. R. Leone, P. S. Cremer, J. T. Groves, M. A. Johnson, and G. Richmond, eds.), vol. 61 of *Annual Review of Physical Chemistry*, pp. 149–170, Palo Alto: Annual Reviews, 2010.

[93] P. Zawadzki, J. Rossmeisl, and K. W. Jacobsen, "Electronic hole transfer in rutile and anatase tio$_2$: Effect of a delocalization error in the density functional theory on the charge transfer barrier height," *Phys. Rev. B*, vol. 84, p. 121203, Sep 2011.

[94] N. A. Deskins and M. Dupuis, "Electron transport via polaron hopping in bulk tio2: A density functional theory characterization," *Physical Review B*, vol. 75, no. 19, 2007.

[95] N. A. Deskins and M. Dupuis, "Intrinsic hole migration rates in tio2 from density functional theory," *Journal of Physical Chemistry C*, vol. 113, no. 1, pp. 346–358, 2009.

[96] S. Ong, V. Chevrier, and G. Ceder, "Comparison of small polaron migration and phase separation in olivine limnpo$_4$ and lifepo$_4$ using hybrid density functional theory," *Phys. Rev. B*, vol. 83, p. 075112, Feb 2011.

[97] C. Ouyang, Y. Du, S. Shi, and M. Lei, "Small polaron migration in lixmn2o4: From first principles calculations," *Physics Letters A*, vol. 373, pp. 2796–2799, Jul 2009.

[98] A. Rohrbach, J. Hafner, and G. Kresse, "Ab initio study of the (0001) surfaces of hematite and chromia: Influence of strong electronic correlations," *Physical Review B*, vol. 70, no. 12, 2004.

[99] G. Rollmann, P. Entel, A. Rohrbach, and J. Hafner, "High-pressure characteristics of alpha-fe2o3 using dft plus u," *Phase Transitions*, vol. 78, no. 1-3, pp. 251–258, 2005.

[100] M. Catti, G. Valerio, and R. Dovesi, "Theoretical-study of electronic, magnetic, and structural-properties of alpha-fe2o3 (hematite)," *Physical Review B*, vol. 51, no. 12, pp. 7441–7450, 1995.

[101] D. Benjelloun, J. P. Bonnet, J. P. Doumerc, J. C. Launay, M. Onillon, and P. Hagenmuller, "Anisotropy of the electrical-properties of iron-oxide alpha-fe2o3," *Materials Chemistry and Physics*, vol. 10, no. 6, pp. 503–518, 1984.

[102] E. Kren, P. Szabo, and G. Konczos, "Neutron diffraction studies on (1-x)fe2o3 - xrh2o3 system," *Physics Letters*, vol. 19, no. 2, pp. 103–, 1965.

[103] R. L. Blake, Hessevic.Re, T. Zoltai, and L. W. Finger, "Refinement of hematite structure," *American Mineralogist*, vol. 51, no. 1-2, pp. 123–, 1966.

[104] B. Meredig, A. Thompson, H. A. Hansen, C. Wolverton, and A. van de Walle, "Method for locating low-energy solutions within dft plus u," *Physical Review B*, vol. 82, no. 19, 2010.

[105] J. R. Reimers and N. S. Hush, "Electronic-properties of transition-metal complexes determined from electroabsorption (stark) spectroscopy .2. mononuclear complexes of ruthenium(ii)," *Journal of Physical Chemistry*, vol. 95, no. 24, pp. 9773–9781, 1991.

[106] J. D. Tucker, R. Najafabadi, T. R. Allen, and D. Morgan, "Ab initio-based diffusion theory and tracer diffusion in ni-cr and ni-fe alloys," *Journal of Nuclear Materials*, vol. 405, no. 3, pp. 216–234, 2010.

[107] E. De Grave, L. H. Bowen, D. D. Amarsiriwardena, and R. E. Vandenberghe, “57fe mossauer effect study of highly substituted aluminum hematites: determination of the magnetic hyperfine field distributions,” *Journal of Magnetism and Magnetic Materials*, vol. 72, no. 2, pp. 129–140, 1988.

[108] E. Wimmer, W. Wolf, J. Sticht, P. Saxe, C. B. Geller, R. Najafabadi, and G. A. Young, “Temperature-dependent diffusion coefficients from ab initio computations: Hydrogen, deuterium, and tritium in nickel,” *Physical Review B*, vol. 77, no. 13, 2008.

[109] R. Grau-Crespo, A. Y. Al-Baitai, I. Saadoune, and N. H. De Leeuw, “Vacancy ordering and electronic structure of gamma-fe(2)o(3) (maghemite): a theoretical investigation,” *Journal of Physics-Condensed Matter*, vol. 22, no. 25, 2010.

[110] F. Zhou and G. Ceder, “First-principles determination of charge and orbital interactions in fe(3)o(4),” *Physical Review B*, vol. 81, no. 20, 2010.

[111] H. T. Jeng, G. Y. Guo, and D. J. Huang, “Charge-orbital ordering in low-temperature structures of magnetite: Gga+u investigations,” *Physical Review B*, vol. 74, no. 19, 2006.

[112] Z. Lodziana, “Surface verwey transition in magnetite,” *Physical Review Letters*, vol. 99, no. 20, 2007.

[113] G. K. H. Madsen and P. Novak, “Charge order in magnetite. an lda+u study,” *Europhysics Letters*, vol. 69, no. 5, pp. 777–783, 2005.

[114] M. J. Wenzel and G. Steinle-Neumann, “Nonequivalence of the octahedral sites of cubic fe3o4 magnetite,” *Physical Review B*, vol. 75, no. 21, 2007.

[115] M. S. Senn, I. Loa, J. P. Wright, and J. P. Attfield, “Electronic orders in the verwey structure of magnetite,” *Physical Review B*, vol. 85, no. 12, 2012.

[116] H. P. Pinto and S. D. Elliott, “Mechanism of the verwey transition in magnetite: Jahn-teller distortion and charge ordering patterns,” *Journal of Physics-Condensed Matter*, vol. 18, no. 46, pp. 10427–10436, 2006.

[117] N. J. Mosey, P. Liao, and E. A. Carter, “Rotationally invariant ab initio evaluation of coulomb and exchange parameters for dft+u calculations,” *Journal of Chemical Physics*, vol. 129, no. 1, 2008.

[118] I. Chamritski and G. Burns, “Infrared- and raman-active phonons of magnetite, maghemite, and hematite: A computer simulation and spectroscopic study,” *Journal of Physical Chemistry B*, vol. 109, no. 11, pp. 4965–4968, 2005.

[119] M. Blanchard, M. Lazzeri, F. Mauri, and E. Balan, “First-principles calculation of the infrared spectrum of hematite,” *American Mineralogist*, vol. 93, no. 7, pp. 1019–1027, 2008.

[120] T. D. Glotch, P. R. Christensen, and T. G. Sharp, “Fresnel modeling of hematite crystal surfaces and application to martian hematite spherules,” *Icarus*, vol. 181, no. 2, pp. 408–418, 2006.

[121] S. Onari, T. Arai, and K. Kudo, “Ir lattice-vibrations and dielectric-dispersion in alpha-fe2o3,” *Physical Review B*, vol. 16, no. 4, pp. 1717–1721, 1977.

[122] S. H. Shim and T. S. Duffy, “Raman spectroscopy of fe2o3 to 62 gpa,” *American Mineralogist*, vol. 87, no. 2-3, pp. 318–326, 2002.

[123] I. R. Beattie and T. R. Gilson, “Single-crystal raman spectra of nearly opaque materials - iron(iii) oxide and chromium(iii) oxide,” *Journal of the Chemical Society a -Inorganic Physical Theoretical*, no. 6, pp. 980–, 1970.

[124] A. U. Gehring and A. M. Hofmeister, “The transformation of lepidocrocite during heating - a magnetic and spectroscopic study,” *Clays and Clay Minerals*, vol. 42, no. 4, pp. 409–415, 1994.